Correspondence to:
Y. Liu and Y. Liu,
yliu@ucar.edu;
yueliu@ucar.edu

Mechanisms for a Record-Breaking Rainfall in the Coastal Metropolitan City of Guangzhou, China: Observation Analysis and Nested Very Large Eddy Simulation With the WRF Model

Yongjie Huang[1,2] iD, Yubao Liu[1,3] iD, Yuewei Liu[1], Huaiyu Li[4], and Jason C. Knievel[1]
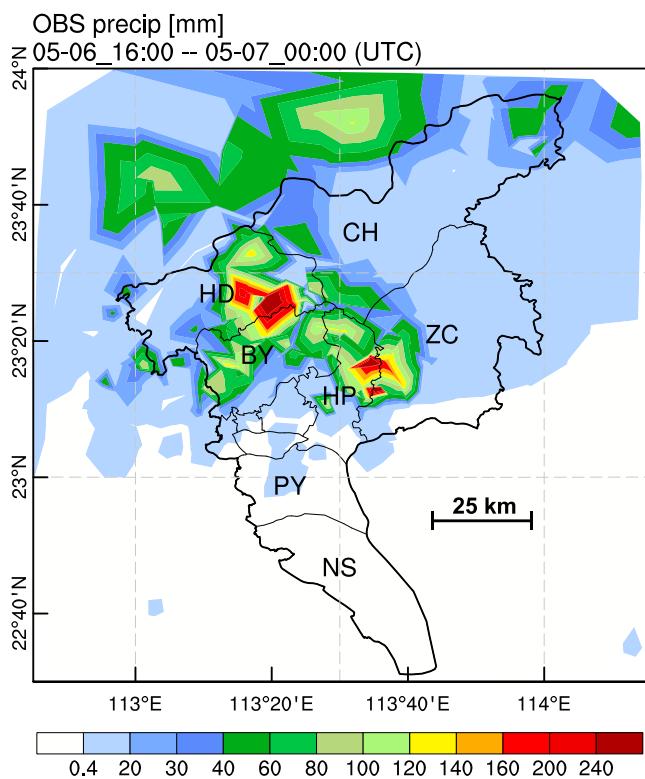
[1]National Center for Atmospheric Research, Boulder, CO, USA, [2]School of Meteorology, University of Oklahoma, Norman, OK, USA, [3]School of Atmospheric Physics, Nanjing University of Information Science and Technology, Nanjing, China, [4]Guangzhou Meteorological Observatory, Guangzhou, China

Abstract Record-breaking rainfall of 524.1 mm in 24 hr occurred in the coastal metropolitan city of Guangzhou, China, during 6–7 May 2017 and caused devastating flooding. Observation analysis and a nested very large eddy simulation (VLES) with Weather Research and Forecasting (WRF) model were conducted to investigate various factors that contributed to the heavy rainfall, including synoptic weather pattern, topographic effects, cold pool, and urban effects. First, the warm and moist southerly flow in the lower troposphere over the trumpet-shaped topography of the Pearl River Delta continuously provided fuel for the development of the severe rainfall. Consequently, the southerly flow from the sea in the south strengthened with the development of the convection. Meanwhile, the precipitation-produced weak cold pool supported a stationary outflow boundary, where new convective cells were continuously initiated and drifted downstream. The interaction between the cold outflows and the warm moist southerly flows in the lower troposphere formed a back-building convective system, which produced local persistent heavy rainfall that lasted for more than 5 hr and reached record levels. Sensitivity experiments in which the urban area was removed from the model indicate that the urban forcing affected the timing and location of convective initiation and helped concentrate the maximum rain core. The nested WRF-LES successfully simulated this heavy rainfall, and the model's advantages are noted for forecasting such local severe weather.

1. Introduction

Over 50% of the world's population lives in urban areas, and this proportion is still growing (Grimm et al., 2008). By 2030, populations in 41 cities are projected to exceed 10 million, and 60% of world's population will be urban (United Nations, 2016). Therefore, the urban weather forecast will become more and more important. Convective storms occurring in urban areas can induce severe flooding and cause serious hazards to lives and property. Severe convective storms that occurred in Houston, TX, USA, on 19 April 2016 brought historic floods, and Houston faced catastrophic losses after the flood (http://floodlist.com/america/usa/texas-floods-deaths-houston-state-of-disaster). Record-breaking rainfall caused by severe storms occurred in Guangzhou, China, on 7 May 2017, causing serious floods, loss of life, and extensive property damage (http://floodlist.com/asia/china-guangzhou-floods-may-2017).

Most metropolises in the world are located in coastal zones (Balk et al., 2008). Land surfaces of these metropolises, such as Houston, New York, and Guangzhou, are heterogeneous and complex, comprising coastal terrain, land-sea boundaries, and urban built-up areas. These complex underlying surfaces can significantly influence local wind circulations and convection and make weather forecasting, especially of local severe convective storms, very challenging. Many observational and modeling studies have shown the impacts of urban land cover on temperature, moisture, air flows, and on the location, distribution, and intensity of convective precipitation in urban and surrounding areas (Dou et al., 2015; Han & Baik, 2008; Miao et al., 2011; Niyogi et al., 2011; Shepherd, 2005; Seino et al., 2018). Bornstein and Lin (2000) conducted an observational analysis to show that the urban heat island (UHI) induced a convergence zone that initiated storms in Atlanta in the period from 26 July to 3 August 1996. The numerical simulation conducted by Miao et al. (2011) on a heavy rainfall event in Beijing in the summer of 2006 confirmed that the urban effect of Beijing played an important role in storm movement and rainfall amount.

Figure 1. Observed accumulated precipitation (mm) from rain gauges in Guangzhou region from 1600 UTC 06 (0000 LST 07) May to 0000 UTC (0800 LST) 07 May 2017. The thick and thin solid black lines represent Guangzhou City and its district borders, respectively. Tick marks are included every 50 km. The initials in the figure are as follows: HD = Huadu District; CH = Conghua District; BY = Baiyun District; HP = Huangpu District; ZC = Zengcheng District; PY = Panyu District; NS = Nansha District.

A high-resolution numerical model is necessary for understanding the highly local urban precipitation features and the existence of highly heterogeneous land surface forcing (land uses and terrain). Bryan et al. (2003) simulated squall lines and recommended a grid spacing of O(100 m) for simulating deep moist convection. Kang and Bryan (2011) conducted idealized large-eddy simulations (LESs) to investigate convection initiation due to heterogeneous surface fluxes and pointed out that increasing the model horizontal grid resolution is beneficial for forecasting convective initiation. The turbulence-resolving LES mode of the Weather Research and Forecasting model (hereafter referred to as WRF-LES) has been used for real case studies, and with positive results beneficial to the study of different topics such as wind energy (Liu et al., 2011), orographic cloud seeding (Chu et al., 2014, 2017; Xue et al., 2016, 2017), and deep convection (Heath et al., 2017; Parodi & Tanelli, 2010). These studies indicate that WRF-LES is promising for fine-scale weather forecasts.

Although the understanding of urban weather and numerical weather prediction models for urban weather modeling have been improving significantly, precipitation forecast, especially quantitative precipitation forecast, in urban areas is still a formidable challenge for weather forecasters. For example, the local official forecast division predicted a moderate shower over the coastal metropolitan city Guangzhou, China, during 6–7 May 2017, but it turned out to be a record-breaking rainfall (a maximum daily rainfall of 524.1 mm breaking the previous record 477.4 mm at Paitan Town of Guangzhou on 23 May 2014) that caused devastating flooding. Apparently, there were some unusual driving factors for the heavy rain formation that were not properly understood or readily accessible to weather forecasters during their routine forecasting practices.

This study aims to investigate the mechanisms for this record-breaking rainfall. We conducted detailed observational analysis and performed WRF-LES modeling with data assimilation to explore the potential for local severe storm forecasting, and we hope to provide valuable guidance for operational forecasters for such severe storms. Weather analysis is based on observational data. High-resolution WRF-LES sensitivity experiments are carried out to investigate the roles of synoptic weather, mesoscale topographic forcing, cold pools, and urban effects during this heavy rainfall. The paper is organized as follows. Section 2 describes the characteristics of the heavy convective rainfall and its synoptic conditions. The data used for weather analysis and model setup are given in section 3. We validate the WRF-LES simulation, and the results are presented in sections 4 and 5, respectively. In section 6 are the findings and summary of the study.
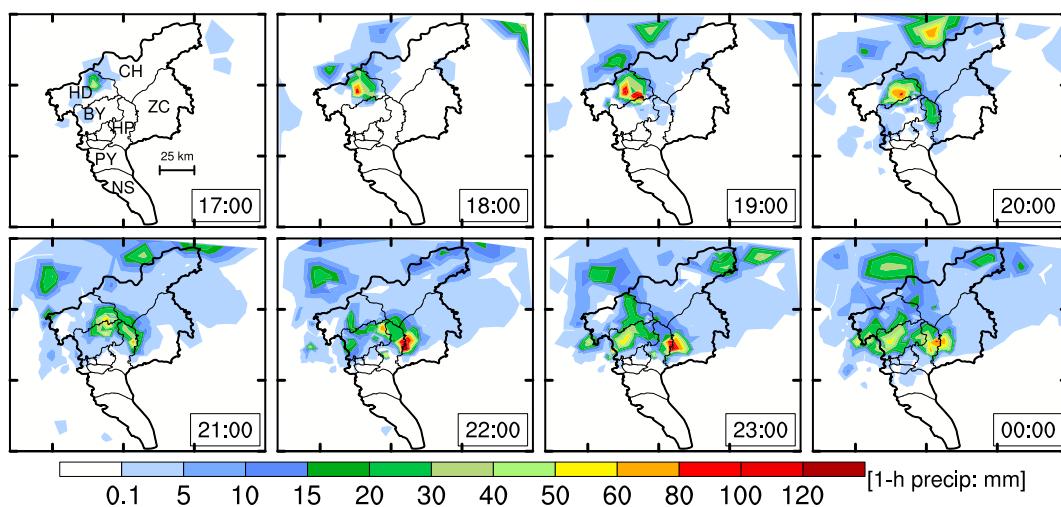
2. Precipitation and Synoptic Conditions

The record-breaking torrential downpours in the metropolitan region of Guangzhou, southern China, during 6–7 May 2017 included a record daily rainfall of 524.1 mm at Jiulong Town, Huangpu (HP) District, Guangzhou. Figures 1 and 2 show the accumulated precipitation and hourly precipitation in Guangzhou from 1600 UTC 06 (0000 LST 07, local standard time LST = UTC + 8 hr) May to 0000 UTC (0800 LST) 07 May 2017, respectively. The precipitation was very intense, quasi-stationary, long-lived, and highly local (Figure 1).

The spatiotemporal distribution of hourly precipitation (Figure 2) shows that it was mainly located within Guangzhou City, which suggests that the torrential rainfall was highly convective. By 2000 UTC 06 (0400 LST 07) May, the rainfall was mainly concentrated in Huadu District (HD). Thereafter, the strong rain cores moved to Baiyun (BY), HP, and Zengcheng (ZC) Districts with the convection moving southeastward and merging with newly generated convective cells. All hourly rainfall exceeded 60 mm during 1800 UTC 06 (0200 LST 07) to 0000 UTC (0800 LST) 07, and the maximum hourly accumulated rainfall was over

Figure 2. Observed hourly accumulated rainfall (mm) from rain gauges in the Guangzhou region from 1700 UTC 06 (0100 LST 07) to 0000 UTC 07 (0800 LST 07) May 2017 at 1-hr intervals. The thick and thin solid black lines represent Guangzhou City and its district borders, respectively. Tick marks are included every 50 km. The initials in the first figure are the same as those in Figure 1.

120 mm at 1900 UTC 06 (0300 LST 07), 2200 UTC 06 (0600 LST 07), and 2300 UTC 06 (0700 LST 07) May. The maximum hourly accumulated rainfall (184.4 mm) during this event was recorded at Xintang Town, ZC, at 2200 UTC 06 (0600 LST 07) May. The slow movement and the long duration of the convective system with intense rainfall rates resulted in large accumulations in Guangzhou.

This event took place under relatively slowly evolving synoptic conditions. The subtropical high was mainly located over the northwestern Pacific Ocean, and mainland China was dominated by westerly flow in the upper troposphere (not shown). In the lower troposphere (Figure 3), there were two cold highs. One was located over the central China, and the other was over the East China Sea. Under these synoptic patterns, there were easterly winds over the South China Sea in the lower troposphere. Southerly winds developed and were sustained over the southern coastal regions of Guangdong Province (Figure 3). Strong winds were found mainly in the lower levels, especially at the level of 975 hPa (Figures 3a1 and 3a2). This circulation pattern was maintained before and during the precipitation (Figure 3), and continuously transported moisture, warm air, and energy to the region of the heavy precipitation.
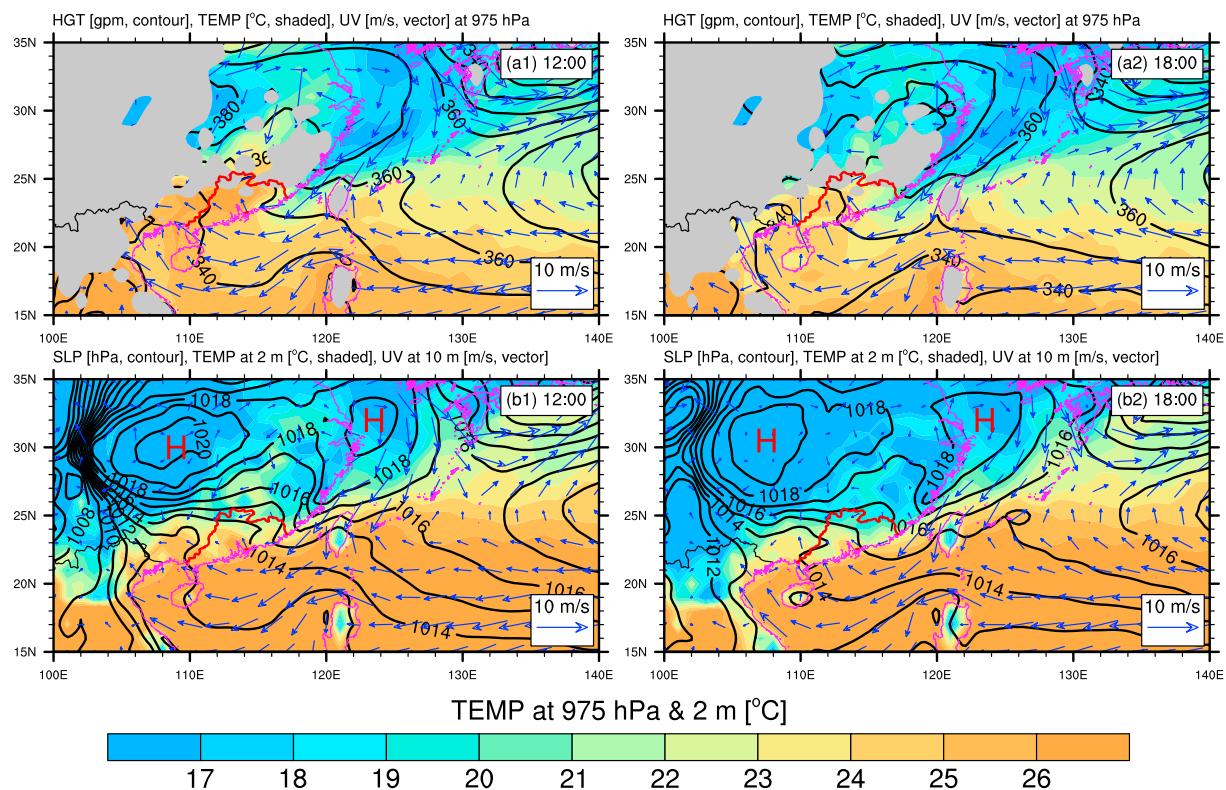
3. Data and Model

3.1. Data

The observations used in this study include conventional meteorological data from a dense network of automatic weather stations (e.g., air temperature at 2 m, winds at 10 m, and rain gauge data), radiosondes, wind profilers, and radars from the Meteorological Bureau of Shenzhen Municipality, China. These observations are used for case analysis, data assimilation into the model, and model validation. Figure 4 shows the locations of dense automatic weather stations used in this study. The National Centers for Environmental Prediction (NCEP) FNL (Final) Operational Model Global Tropospheric Analysis (NCEP-FNL) available every 6 hr with resolution of 1° × 1° on 31 vertical levels (http://rda.ucar.edu/datasets/ds083.2/) is used to analyze synoptic weather (Figure 3) and drive the WRF model as well. For the initial conditions of land surface model coupled with the WRF model, we used the NCEP Global Land Data Assimilation System (GLDAS) Noah Land Surface Model data set V2.1 available every 3 hr with resolution of 0.25° × 0.25° (Beaudoing & Rodell, 2016; https://disc.sci.gsfc.nasa.gov/datacollection/GLDAS_NOAH025_3H_V2.1.html).

3.2. WRF Modeling Design

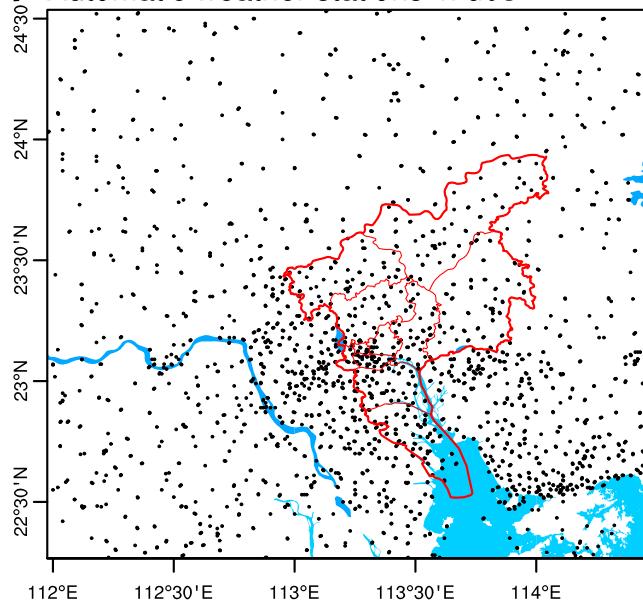In this study, the WRF v3.8.1 is configured with 3 one-way nested domains at 4.5-, 1.5-, and 0.5-km horizontal grid spacings (Figure 5a). All domains use 51 vertical levels with stretching in the lowest 2 km. The Shin-Hong scale-aware planetary boundary layer (PBL) scheme (Shin & Hong, 2015) is used for the 4.5- and 1.5-km domains. The 0.5-km domain is configured in LES mode, so the PBL parameterization

Figure 3. (a1, a2) Geopotential height (black contours in gpm), air temperature (color shading in °C), and wind vectors (blue in m/s) at 975-hPa levels and (b1, b2) mean sea level pressure (black contours in hPa), air temperature (color shading in °C) at 2 m above ground level, and wind vectors (blue in m/s) at 10 m above ground level at 1200 UTC (2000 LST) 06 and 1800 UTC 06 (0200 LST 07) May, respectively. The gray shaded areas indicate the values that are missing due to the elevation. All these fields are from the NCEP-FNL data set. The red and magenta solid lines represent the Guangdong Province border and land-sea border, respectively.
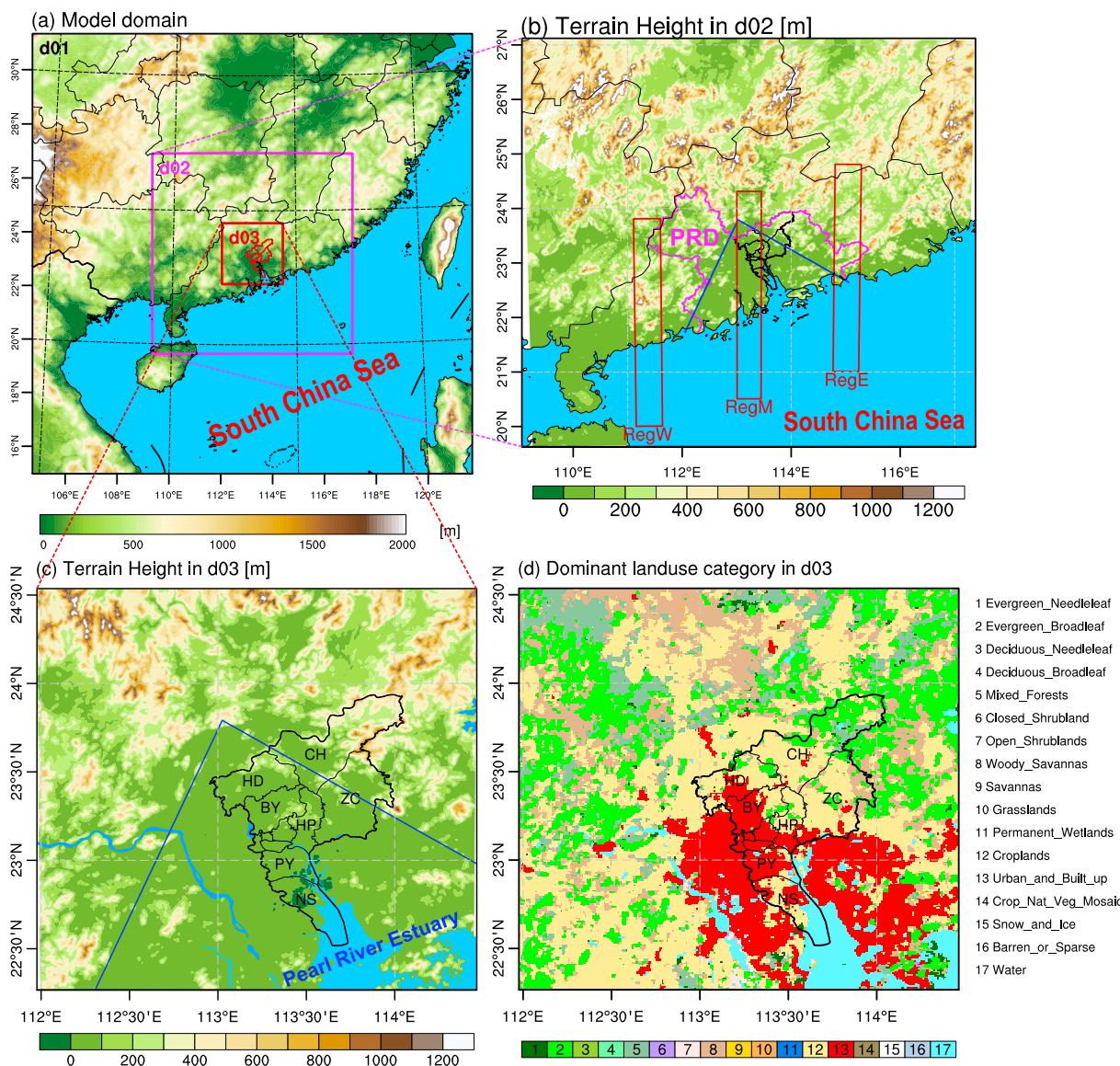

Figure 4. Automatic weather stations (black points) in domain 3 (d03) of the Weather Research and Forecasting model setup. The blue shaded areas indicate water. The thick and thin solid red lines represent Guangzhou City and its district borders, respectively.

scheme is not activated. However, we recognize that a grid interval of 0.5 km is coarse compared to that in traditional LES, so we use the term *very large eddy simulation* (VLES) to describe our application of the model. A 1.5-order turbulent kinetic energy closure is used in the WRF-LES simulation for the subgrid-scale model. Although the 0.5-km grid spacing falls within the "terra incognita" or "gray zone" range (i.e., 0.1–1 km) in modeling the convective boundary layer (Wyngaard, 2004), some studies (Heath et al., 2017; Parodi & Tanelli, 2010) have shown that WRF-LES in the terra incognita range can simulate deep convective processes reasonably. We also performed experiments with the PBL parameterization scheme activated in the 0.5-km domain. We found that the simulation in LES mode more closely resembles the observations than does the simulation with the PBL parameterization scheme (Figure S1). Other physical parameterization schemes are the same for all three domains, including RRTMG (the revised Rapid Radiative Transfer Model) longwave and shortwave radiation scheme (Iacono et al., 2008), Unified Noah land surface scheme (Tewari et al., 2004), and MM5 (the Fifth-Generation National Center for Atmospheric Research / Penn State Mesoscale Model) Monin-Obukhov similarity scheme (Zhang & Anthes, 1982). Cumulus parameterization scheme is not activated.
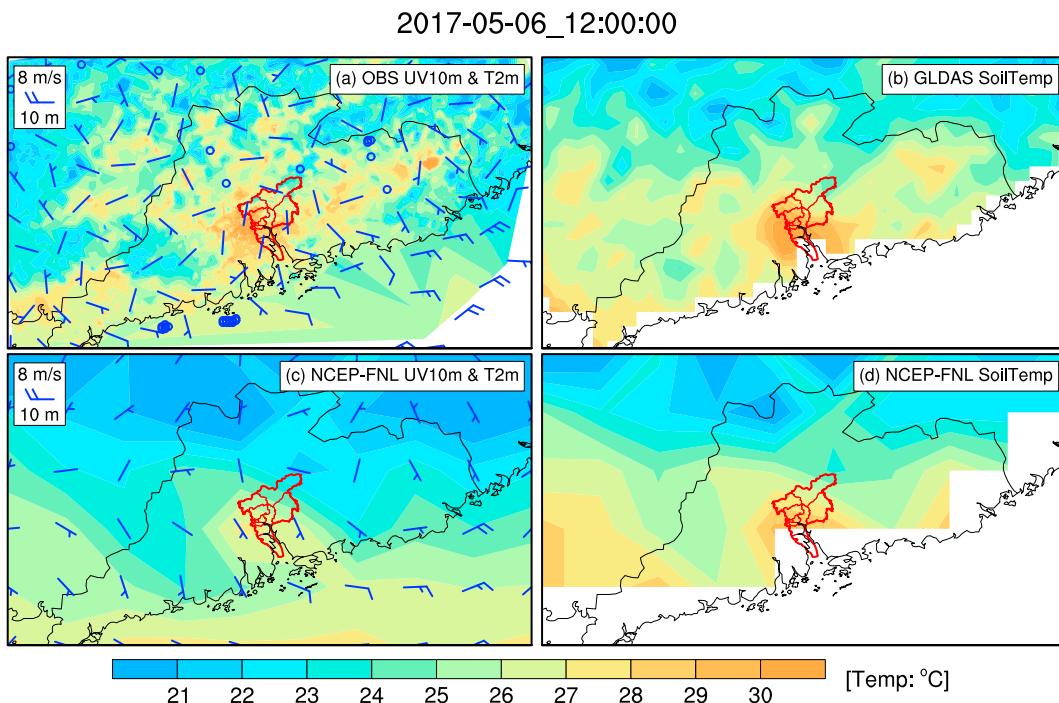
Global analysis data including NCEP operational Global Forecast System analysis data at 0.25° × 0.25° and 0.5° × 0.5° grid intervals, NCEP-FNL data and ERA-Interim data at a 0.7° grid interval were tested for

Figure 5. (a) The model's domain configuration (color shaded fields represent terrain elevation, in m), terrain elevation (m) in (b) domain 2 (d02) and (c) domain 3 (d03), and (d) dominant land use category in d03 (each category is described by the text on the right side of the figure). The horizontal grid spacings of d01, d02, and d03 are 4.5, 1.5, and 0.5 km, respectively. The red rectangles (RegW, RegM, and RegE) in (b) display the positions of cross sections shown in Figure 12. The red administrative boundaries in (a) and black administrative boundaries in (b)–(d) represent Guangzhou City and its districts. The magenta line in (b) represents the border of Pearl River Delta (PRD). The blue thick lines in (b) and (c) indicate the trumpet-shaped topography (more specifically, the bell of a trumpet) of PRD. The initials in (c) and (d) are the same as those in Figure 1.

deriving initial and boundary conditions (ICs and BCs, respectively) for the WRF simulations. Sensitivity experiments on microphysical parameterization schemes including the WRF single-moment 6-class microphysics (WSM6) scheme (Hong & Lim, 2006), Thompson two-moment scheme (Thompson et al., 2008) and Morrison two-moment scheme (Morrison et al., 2009) were also conducted. Results vary in the simulation of radar reflectivity and precipitation when compared with those of observed radar reflectivity and precipitation. The simulation with NCEP-FNL data for ICs and BCs and WSM6 for microphysical parameterization is used for this study.

GLDAS analysis data were evaluated in order to properly consider the urban land surface properties. Figure 6 shows air temperature at 2 m above ground level (AGL) and wind fields at 10 m AGL from observation and the NCEP-FNL data set, and soil temperature at 10 cm below the surface from GLDAS and the

2017-05-06_12:00:00

Figure 6. Air temperature (shaded in °C) at 2 m above ground level and wind fields (wind barbs in m/s) at 10 m above ground level of the (a) observation analysis and (c) NCEP-FNL, and soil temperature (shaded in °C) at 10 cm below ground level of (b) GLDAS and (c) NCEP-FNL at 1200 UTC (2000 LST) 06 May 2017. The thin solid black lines represent Guangdong Province borders. The thick and thin solid red lines mark Guangzhou City and its districts, respectively.
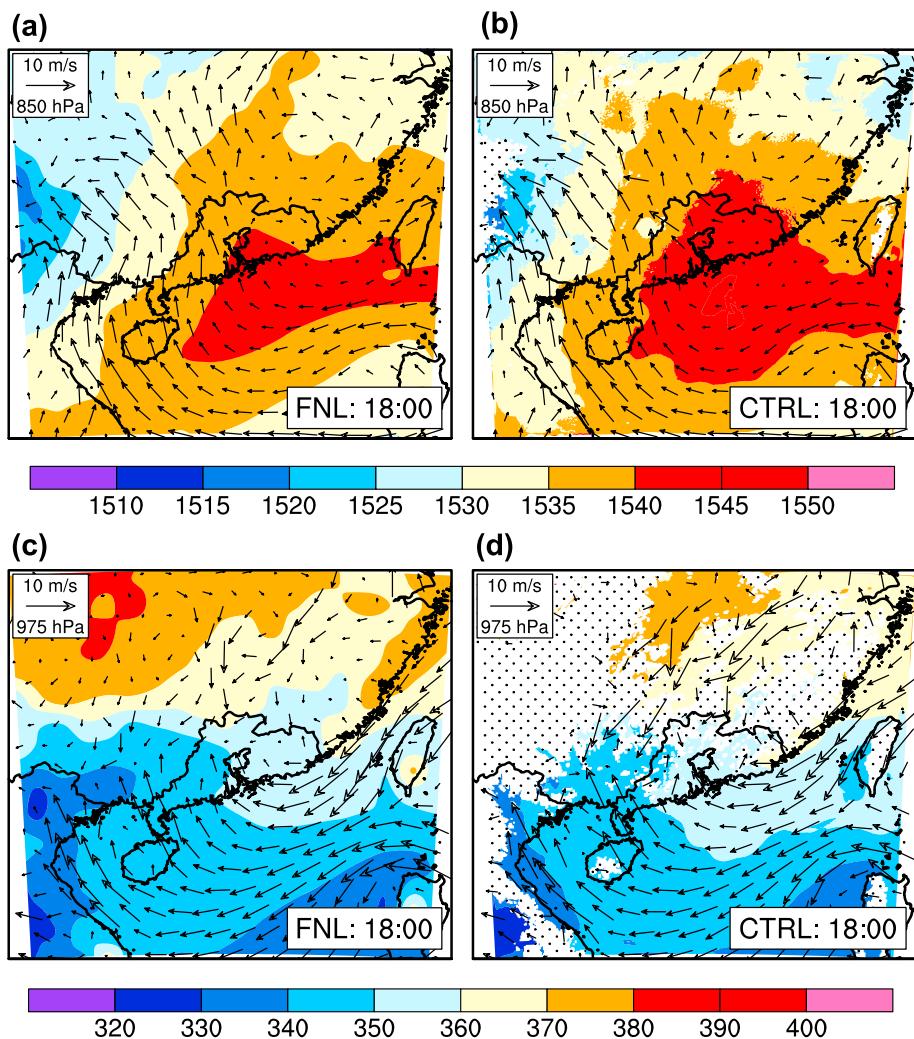
NCEP-FNL data set at 1200 UTC (2000 LST) 06 May 2017, respectively. The air temperature and wind fields of the NCEP-FNL data set resemble the observed (Figures 6a and 6c), while the soil temperature distribution of GLDAS is more similar to that of the observed air temperature than that of NCEP-FNL. Moreover, GLDAS has higher resolution than has NCEP-FNL. In the simulation, canopy moisture content, soil moisture, and soil temperature from GLDAS were used to initialize the Noah land surface model. Land use is interpolated from 21-class MODIS (Moderate Resolution Imaging Spectroradiometer) data set at 30-arcsec resolution; sea surface temperature is from NCEP-FNL.

The nested VLES was initialized at 1200 UTC (2000 LST) 06 May 2017 and integrated for 12 hr to test its capability simulating the storm. To achieve a realistic simulation, surface observations, soundings, and wind profiles were assimilated by using the WRF-based real time four-dimensional data assimilation and forecasting system, developed at the Research Application Laboratory of the National Center for Atmospheric Research (Huang et al., 2018; Liu, Warner, Bowers, et al., 2008, Liu, Warner, Astling, et al., 2008). Data assimilation was performed between 1200 UTC (2000 LST) 06 and 0000 UTC (0800 LST) 07 May 2017 in the coarse domains (4.5 and 1.5 km) and also 1200 UTC (2000 LST) 06 May to 1600 UTC 06 (0000 LST 07) May 2017 (data assimilation was stopped before observed convective initiation) in the 0.5-km domain to evaluate the convective initiation and development in the 0.5-km domain. The simulated data in the 0.5-km domain were written out every 10 min. This experiment is treated as the control experiment (hereafter CTRL). For comparison, we also conducted an experiment without data assimilation in the 0.5-km domain (hereafter NODA).

4. Verification of WRF Simulation

4.1. Mesoscale Circulation

The WRF model reproduced the main mesoscale pattern and flow fields during this severe rainfall event. Figure 7 displays geopotential height and wind vectors at 850- and 975-hPa levels in domain 1 (d01) from NCEP-FNL data and CTRL experiment at 1800 UTC 06 (0200 LST 07) May 2017. At the 850-hPa level, Guangdong Province and its coastal areas were mainly controlled by a high pressure, with a weak
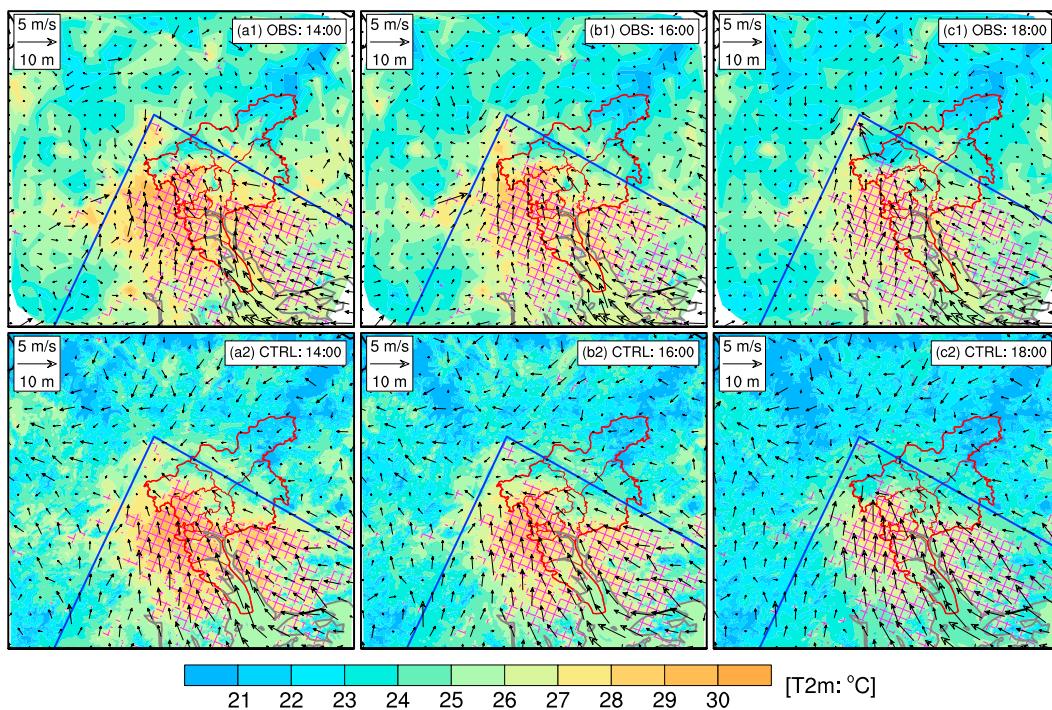
Figure 7. Geopotential height (shaded in gpm) and wind vectors (m/s) at (a, b) 850- and (c, d) 975-hPa level in domain 1 from (a, c) NCEP-FNL data and (b, d) CTRL at 1800 UTC 06 (0200 LST 07) May 2017. The dot fill patterns in (b) and (d) indicate the values that are missing due to the elevation. The black solid lines in mainland China represent Guangdong Province and Guangzhou City borders.

anticyclonic circulation over Guangdong Province, though the simulated high pressure was stronger than that of NCEP-FNL. At the 975-hPa level, a strong northeasterly flow entered into the South China Sea from the Taiwan Strait, driven by the high pressure over the East China Sea. This flow turned northwestward and blew onshore along the southern coast of Guangdong Province. These southerly winds from the South China Sea to the coast of Guangdong persisted during this rainfall event (cf. Figures 3 and 7). As analyzed in detail later, this southerly flow brought abundant moisture and warmth from the South China Sea to the coastal areas of Guangdong, supporting the sustainable development of the severe convective storms over Guangzhou City.

4.2. Surface Meteorological Fields

The simulated surface wind and air temperature, especially those in the urban area within the trumpet-shaped topography (more specifically, the bell of a trumpet) of the Pearl River Delta, resemble the observed. Figure 8 shows observed and simulated (domain 3 [d03] in CTRL) wind at 10 m AGL and air temperature at 2 m AGL from 1400 UTC (2200 LST) 06 to 1800 UTC 06 (0200 LST 07) May 2017. The observed 10-m winds and 2-m air temperature are interpolated from the dense automatic weather station data (cf. Figure 4). The
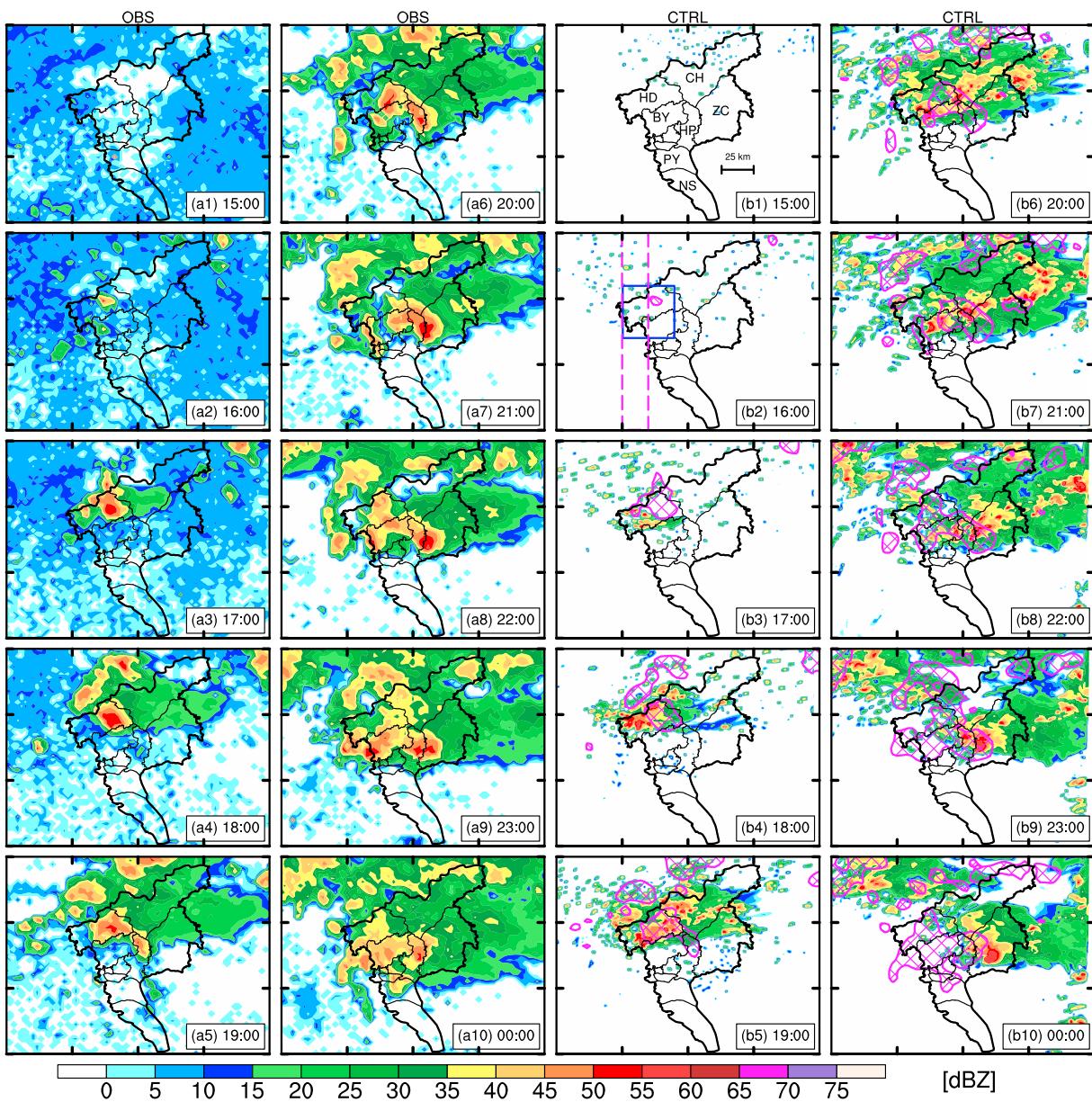
Figure 8. Wind (vectors in m/s) in the (a1–c1) observations and (a2–c2) simulations (in domain 3 of CTRL) at 10 m above ground level and air temperature (shaded in °C) at 2 m above ground level from 1400 UTC (2200 LST) 06 to 1800 UTC 06 (0200 LST 07) May 2017 at 2-hr intervals, respectively. The solid gray lines represent land-sea borders. The thick and thin solid red lines represent Guangzhou City and its district borders, respectively. The diamond fill patterns indicate the urban areas (i.e., category 13 shown in Figure 5d). The blue thick lines indicate the trumpet-shaped topography of the Pearl River Delta.

simulated wind fields and air temperature resemble the observed, especially in the urban area within the trumpet-shaped topography of the Pearl River Delta (Figure 8). The severe local storms occurred within the trumpet-shaped topography region, and the strong, warm, and moist southerly flow in the lower troposphere in the trumpet-shaped topography was a key factor to the record-breaking rainfall (discussed below). The differences in the surface winds outside the trumpet-shaped topography between the simulation and observation (Figure 8) do not affect the main conclusions in this study. Besides, it is still relatively difficult for numerical model to simulate accurate surface winds over the complex mountainous region outside the trumpet-shaped topography (Figure 5b). The southerly winds near the Pearl River estuary (the location shown in Figure 5c) and over the urban region dominated and maintained before and after the convection initiation in HD (1600 UTC 06 [0000 LST 07] May), which was consistent with the result shown in Figures 3 and 7. Besides, the air temperature in the urban area was higher than that in other regions due to the UHI effect (Figure 8). Such surface air temperature contrast helped sustain the southerly wind over the Pearl River estuary. The urban effect in this rainfall event will be discussed in section 5.3.
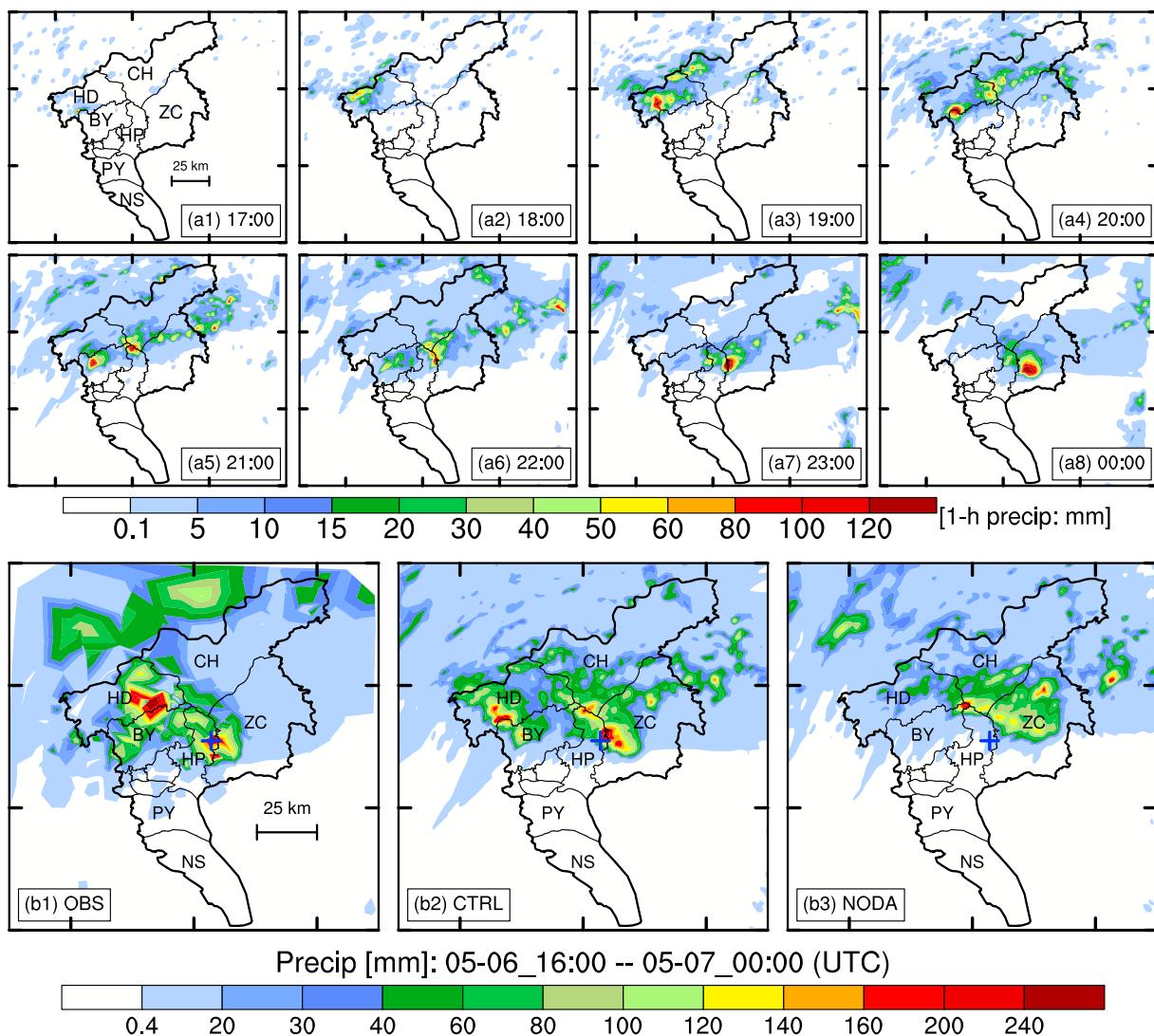
4.3. Radar Reflectivity and Precipitation

Figure 9 displays observed and simulated composite reflectivity from 1500 UTC (2300 LST) 06 May to 0000 UTC (0800 LST) 07 May at 1-hr intervals. From the observation (Figure 9a2), a convective cell (composite reflectivity >35 dBZ) occurred locally in HD at 1600 UTC 06 May (0000 LST 07 May). This was the first observed cell. As this convection was strengthening with time, new convective cells began to develop on the north side of HD from 1700 UTC 06 May (0100 LST 07 May; Figure 9a3). Thereafter, another convective core developed in HP on the southeast side of the old convection (Figure 9a5). Finally, these two areas of convection began to merge over the center of Guangzhou at 2000 UTC 06 May (0400 LST 07 May; Figure 9a6). Meanwhile, some new convective cells formed to the west of Guangzhou, then strengthened while moving eastward, and finally merged with the aforementioned convection over the center of Guangzhou. The resultant large region of merged convection mainly stayed in HD, BY, HP, and ZC from

Figure 9. (a1–a10) Observed and (b1–b10) simulated (in domain 3 of CTRL) composite radar reflectivity (dBZ) over the Guangzhou region from 1500 UTC (2300 LST) 06 May to 0000 UTC (0800 LST) 07 May 2017 at 1-hr interval, respectively. The diamond fill patterns in (b1)–(b10) indicate the areas where observed composite reflectivity is greater than 35 dBZ. The thick and thin solid black lines represent Guangzhou City and its district borders, respectively. Tick marks are included every 50 km. The initials in (b1) are the same as those in Figure 1. The dashed magenta rectangle in (b2) represents the position of cross sections shown in Figure 11.

2100 UTC 06 (0500 LST 07) May to 0000 UTC (0800 LST) 07 May. From the simulated composite reflectivity, it can be seen that a convective cell was also initiated (composite reflectivity >35 dBZ, Figure 9b2) in HD at 1600 UTC 06 (0000 LST 07) May, which is consistent with the observations (Figure 9a2). However, the simulated convection is displaced southwestward from the observation. The model then simulated new cells that grew and merged with the old convection. This process is similar to the observed. In general, the simulated convection was positioned a little more east than observed. The convection over western Guangzhou is not properly simulated.
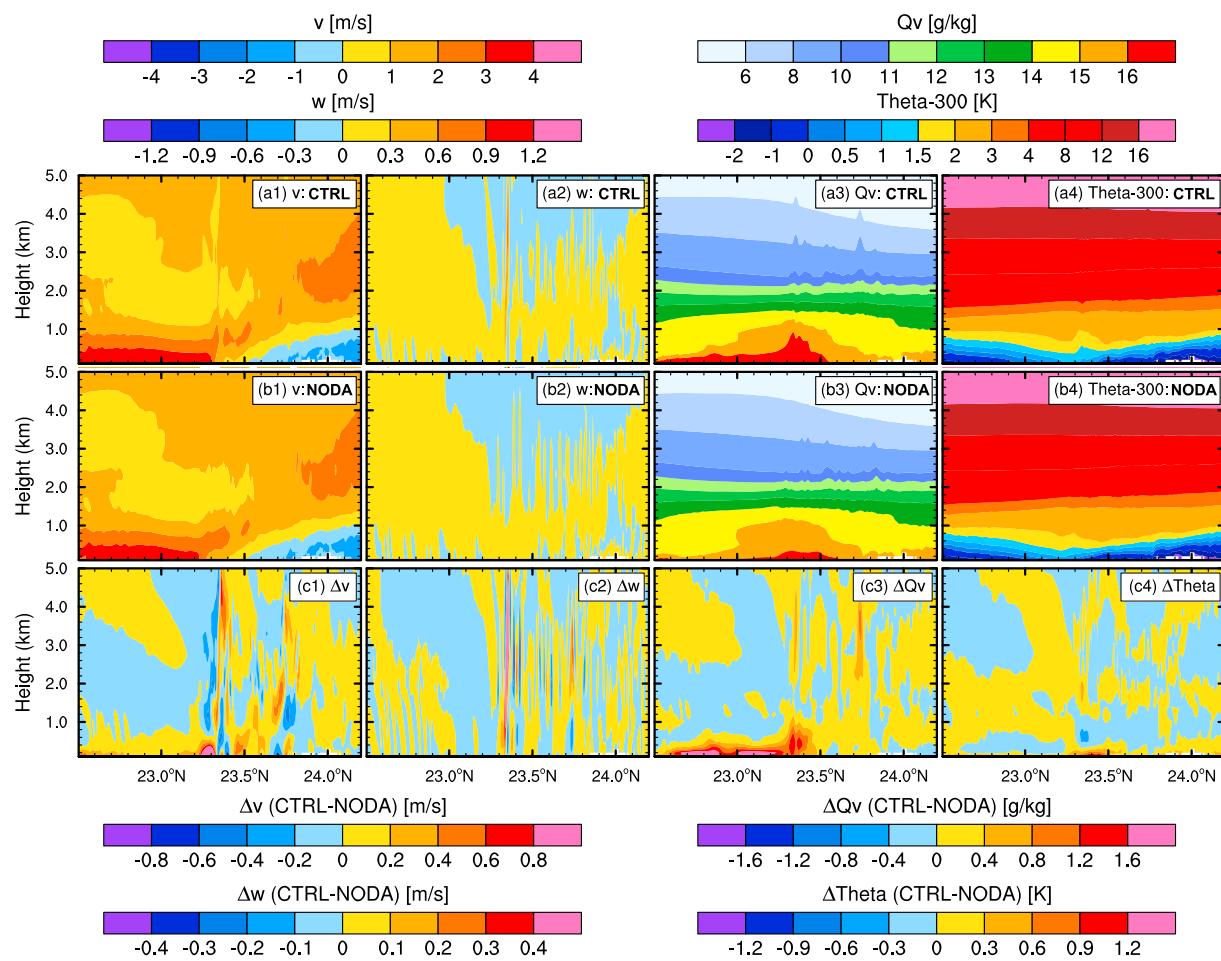
The simulated hourly accumulated precipitation in d03 of CTRL (Figures 10a1–10a8) captured the intensity and scales of the observed precipitation (Figure 2). Before 2000 UTC 06 (0400 LST 07) May, the simulated precipitation mainly distributed in HD (Figures 10a1–10a4), which is consistent with the observations

Figure 10. (a1–a8) Simulated hourly accumulated precipitation (mm) in the Guangzhou region in domain 3 of CTRL experiment from 1700 UTC 06 (0100 LST 07) May to 0000 UTC (0800 LST) 07 May 2017 at 1-hr interval, respectively. Accumulated precipitation (mm) in the (b1) observations, (b2) domain 3 of CTRL, and (b3) NODA in the Guangzhou region from 1600 UTC 06 (0000 LST 07) May to 0000 UTC (0800 LST) 07 May 2017. The blue crosses in (b1)–(b3) indicate the center of maximum accumulated precipitation in the observations. The thick and thin solid black lines represent Guangzhou City and its district borders, respectively. The initials in (a1) and (b1)–(b3) are the same as those in Figure 1. Tick marks are included every 50 km.

(Figure 2). However, the simulated precipitation is shifted southwestward compared to the observations. Thereafter, the precipitation moved slowly to HP and ZC, and the precipitation intensity resembled the observations (all the maximum hourly accumulated rainfall were over 60 mm), and their scales were smaller than 25 km (Figures 2 and 10a5–10a8). The observed and simulated accumulated precipitation in the Guangzhou region from 1600 UTC 06 (0000 LST 07) May to 0000 UTC (0800 LST) 07 May 2017 (Figures 10b1–10b3) shows that the accumulated precipitation of CTRL (Figure 10b2) is more consistent with observations than that of NODA (Figure 10b3), especially the maximum accumulated precipitation center between HP and ZC. The fractions skill score (Roberts & Lean, 2008) of the accumulated precipitation at 60-mm threshold and 25-km (12.5-km radius) horizontal scale is 0.61 for CTRL, while it is 0.29 for NODA. This is an example of how data assimilation can be important for providing more accurate mesoscale weather environments for forecasting convective-scale weather.
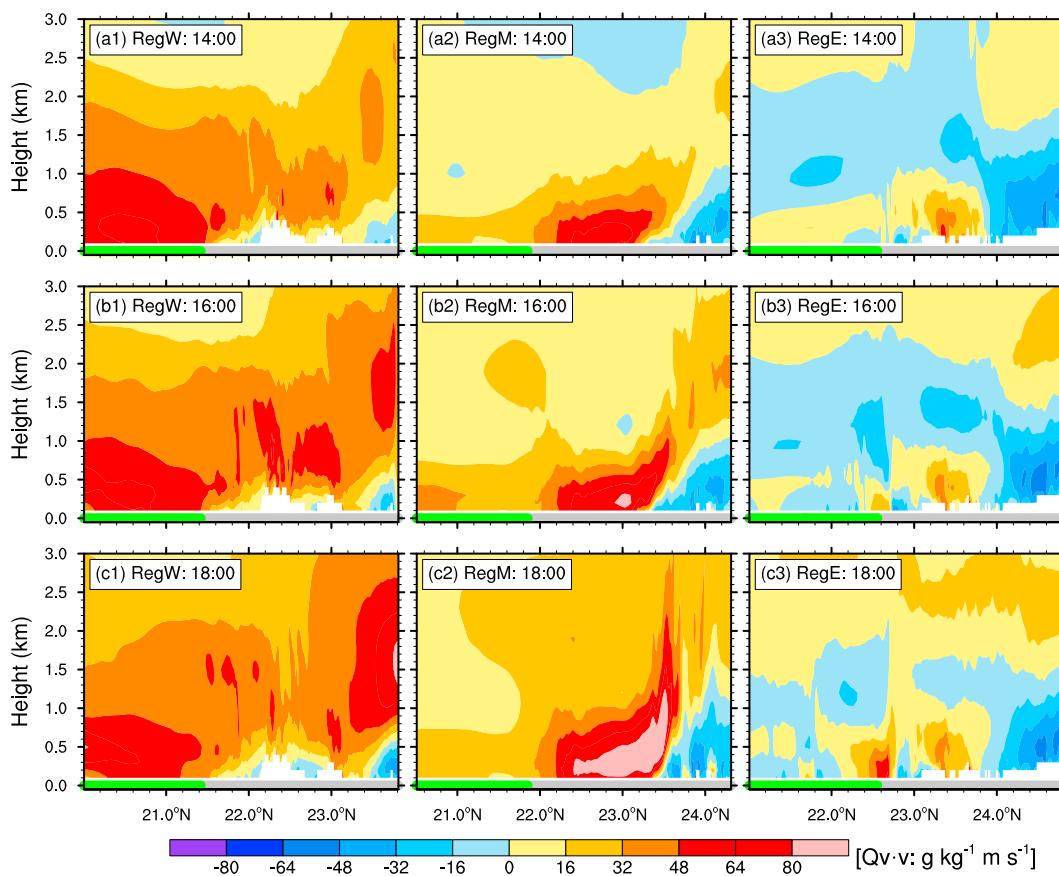
Compared to NODA, the CTRL better captured the warm moist southerly flow and NODA underestimated it. Thus, it is possible to study the impact of the warm moist southerly flow on the heavy rain development by

Figure 11. Height-latitude cross sections of simulated (a1, b1) zonal-mean meridional wind (in m/s), (a2, b2) vertical velocity (in m/s), (a3, b3) water vapor mixing ratio (in g/kg), and (a4, b4) perturbation potential temperature (in K) in the regions shown in Figure 9b2 in domain 3 of (a1–a4) CTRL and (b1–b4) NODA, and (c1–c4) their differences (CTRL − NODA) at 1600 UTC 06 (0000 LST 07) May 2017, respectively. The white areas indicate the values that are missing due to the elevation.

comparing the NODA and CTRL runs. Figure 11 shows the height-latitude cross sections of meridional wind, vertical velocity, water vapor mixing ratio, and perturbation potential temperature in d03 of CTRL and NODA and their differences at 1600 UTC 06 (0000 LST 07) May 2017, the initiation time of the first convection in HD. The winds were mainly southerly from the surface to 5 km to the south of 23.5°N, and strong winds were found below 1 km. In the north, weak northerly wind existed below 1 km (Figures 11a1 and 11b1). Therefore, the moisture flux was convergent in the lower troposphere at around 23.4° N (Figures 11a3 and 11b3). Meanwhile, the perturbation potential temperature fluctuated and had large horizontal gradients in this region (Figures 11a4 and 11b4) and strengthened with time (not shown). Compared to NODA, there are stronger southerly winds (Figure 11c1), more moisture (Figure 11c3), and warmer air (Figure 11c4) near the surface in CTRL, indicating the role of data assimilation in the stronger simulated warm moist southerly wind. Finally, convection was initiated earlier in CTRL than in NODA (vertical velocity shown in Figures 11a2–11c2). Therefore, the stronger warm moist southerly wind in the lower troposphere in CTRL appears to be very important for this severe rainfall event.

Overall, CTRL reasonably simulated the initiation and development of the observed convection and the intensity and scale of precipitation of the heavy rainfall event. In the following section, the mechanisms for the formation of the record precipitation between HP and ZC are analyzed based on the WRF model simulation.
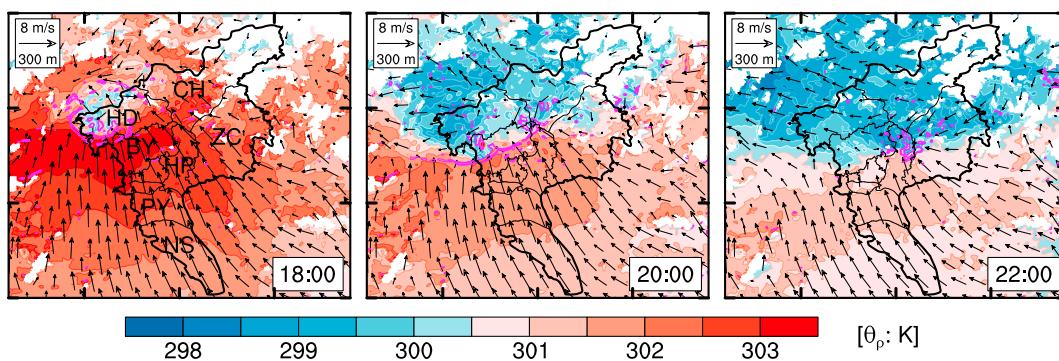
Figure 12. Height-latitude cross section of zonal-mean simulated meridional water vapor flux (shaded in g/kg·m/s) in domain 2 of CTRL in the three regions (RegW, RegM, and RegE) shown in Figure 5b from 1400 UTC (2200 LST) 06 May to 1800 UTC 06 (0200 LST 07) May 2017 at 2-hr intervals, respectively. The white areas indicate the values that are missing due to the elevation. The thick solid lines at 0-km height indicate ocean surface (green) and continent surface (gray).

5. Analysis of Key Factors for the Heavy Rainfall

5.1. Topographic Effects

Guangzhou City is situated in the hinterland of the Pearl River Delta (Figure 5b), which is the low-lying area surrounding the Pearl River estuary (Figure 5c). From the topography of Guangdong Province shown in Figure 5b, the west, north, and east sides of the Pearl River Delta are mountainous, and its south side is opened to the South China Sea. Hence, Guangzhou is located in a trumpet-shaped topography area (Figure 5c), which is favorable for the convergence of air flow and water vapor.

To investigate the effect of topography on this severe torrential rainfall, three regions were selected to study the flow features based on their topography. They are the region to the west of the Pearl River Delta (RegW), the region through Guangzhou City in the middle of the Pearl River Delta (RegM), and the region to the east of the Pearl River Delta (RegE) as marked in Figure 5b. Figure 12 shows the simulated zonal-mean meridional water vapor flux in these three regions in domain 2 (d02) of CTRL at 1400 UTC (2200 LST) 06, 1600 UTC 06 (0000 LST 07), and 1800 UTC 06 (0200 LST 07) May 2017, respectively. Due to the distribution characteristics of circulation, the intensity of the wind blowing toward the shore of southern Guangdong was different along the coast and was particularly strong on the western coast of Guangdong (Figure 7). Therefore, there was stronger meridional moisture flux in RegW compared to those in RegM and RegE over the sea (Figure 12). Southerly moisture flux was enhanced in all these three regions from 1400 UTC (2200 LST) 06 May to 1800 UTC 06 (0200 LST 07) May 2017 (Figure 12). However, moisture flux was blocked by the terrain in RegW and mainly was focused at the southern foot of the mountain near the coast (Figures 12a1–12c1). In RegM, strong southerly moisture flux in the lower troposphere, mainly below 1 km, expanded far inland (Figures 12a2–12c2) to roughly 23.5°N due to the north mountain and northerly wind induced

Figure 13. Simulated wind vectors (m/s), density potential temperature θ_ρ (shaded in K), and vertical velocity (magenta contours, >0.3 m/s) at 300 m above mean sea level from 1800 UTC 06 (0200 LST 07) May to 2200 UTC 06 (0600 LST 07) May 2017 at 2-hr intervals in domain 3 of CTRL, respectively. The white areas indicate the values that are missing due to the elevation. The thick and thin solid black lines represent Guangzhou City and its district borders, respectively. The initials in the first figure are the same as those in Figure 1. Tick marks are included every 50 km.

by high pressure in the north (Figure 7). It was very favorable for the accumulation of water vapor and instability before convective storms were initiated. After initiation (1600 UTC 06 May 2017), southerly moisture flux continued enhancing (Figures 12b2 and 12c2) and providing sufficient water vapor for the development of more convection. Due to the weaker southerly flow and the topographic countercheck, there was weaker southerly moisture flux in RegE region compared to those in RegW and RegM (Figures 12a3–12c3). Therefore, the topographic effect of the Pearl River Delta, which channeled abundant water vapor to the Guangzhou region, is one of the key factors for the initiation and maintenance of these severe storms. The synoptic pattern drove sustaining southerly flow in the Pearl River Delta. Figure 12 also shows that after convection occurred, the convergence in the lower level was enhanced, and the southerly flow strengthened, which brought in plentiful water vapor to support the development of the rainstorm.
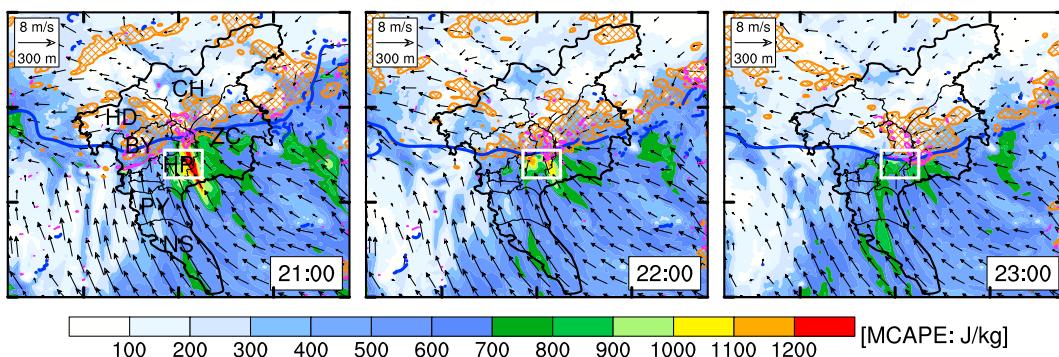
5.2. Development of Sustained Stationary Outflow Boundaries

Evaporation of raindrops in precipitation generates cold air pools in the lower troposphere. Figure 13 shows the simulated wind vectors, density potential temperature θ_ρ, and updraft velocity at 300 m above mean sea level from 1800 UTC 06 (0200 LST 07) May to 2200 UTC 06 (0600 LST 07) May 2017 at 2-hr intervals in d03 of CTRL. Following Emanuel (1994) and Panosetti et al. (2016), θ_ρ is defined as

$$\theta_\rho = \theta \frac{1 + \frac{R_v}{R_d} Q_v}{1 + Q_T},$$

where θ is the potential temperature, R_v and R_d are the gas constants for water vapor and dry air, respectively, Q_v is the water vapor mixing ratio, and $Q_T = Q_v + Q_l + Q_i$ is the net water mixing ratio including liquid and ice water. The value of θ_ρ may be either less or greater than the actual potential temperature θ depending on the relative amounts of water vapor and condensed water. The cold pools are visible as regions of low θ_ρ (low θ and high Q_T; Panosetti et al., 2016) in Figure 13. After the first convection formed in HD (Figure 9), the precipitation intensified (Figure 10), and then cold pools formed and expanded in the lower troposphere (Figure 13). The interaction between the southern cold outflow boundaries and the warm moist southerly flow triggered new updrafts in the front of the cold pools, and new convective cells were initiated (Figures 9 and 13). Therefore, during both the initial convective initiation and the later development, the sustaining warm moist southerly flow in the lower troposphere played the key role.

The cold outflow boundaries were quasi-stationary near HP and ZC (Figure 14), where extreme rainfall occurred (Figure 10). Strong instability (convective available potential energy [CAPE] >700 J/kg) existed persistently in front of the southern cold-pool boundary (Figure 14), supporting development and maintaining of updrafts.
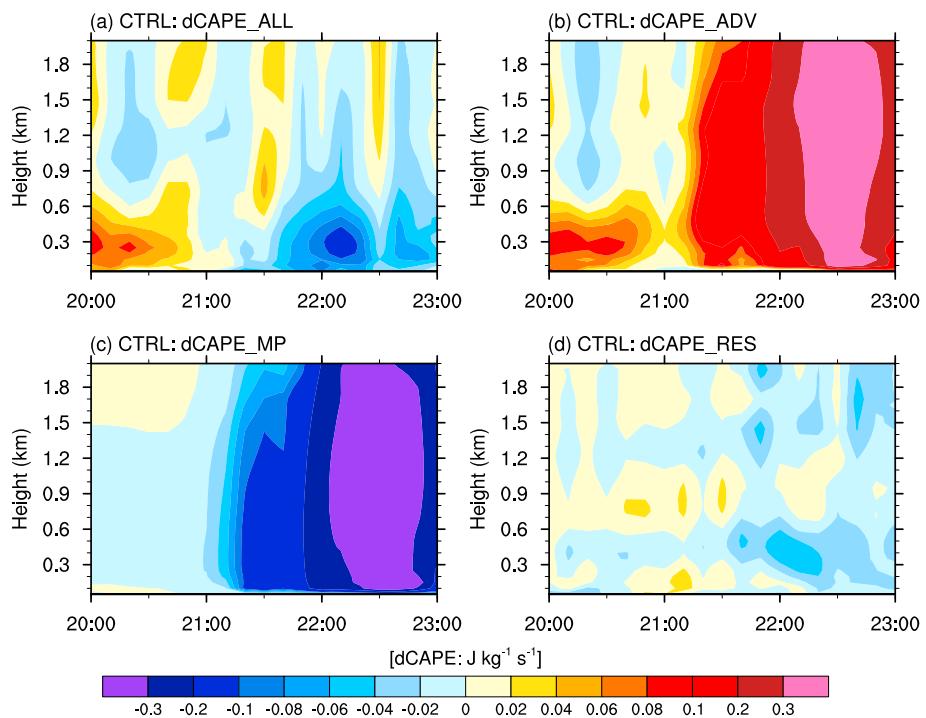
Figure 14. Simulated wind vectors (m/s), density potential temperature θ_ρ (thick blue contour, =300 K) and vertical velocity (magenta contours, >0.3 m/s) at 300 m above mean sea level, composite reflectivity (diamond fill patterns, >35 dBZ), and maximum convective available potential energy (shaded in J/kg) from 2100 UTC 06 (0500 LST 07) May to 2300 UTC 06 (0700 LST 07) May 2017 at 1-hr interval in domain 3 of CTRL, respectively. The white rectangles represent the computational areas for Figure 15. The thick and thin solid black lines represent Guangzhou City and its district borders, respectively. The initials in the first figure are the same as those in Figure 1. Tick marks are included every 50 km.

The rate of change in instability is a more valuable indicator than the instability itself for evaluating the effect on convection (Chen et al., 2014; Zhang, 2002). We computed CAPE generation rates in terms of all forcing (dCAPE_ALL) and its three components: large-scale advective forcing (dCAPE_ADV), microphysical forcing (moisture consumption/latent heating; dCAPE_MP), and the residual forcing (dCAPE_RES). dCAPE_RES includes radiation and surface sensible/latent heat fluxes. The definition of dCAPE_ADV is similar to that used by Xie and Zhang (2000) and Suhas and Zhang (2014), which accounts for the joint impact of large-scale upward motion and horizontal advections of temperature and moisture. dCAPE_MP is determined by the change in temperature and moisture due to microphysical processes. dCAPE_ALL, dCAPE_ADV, dCAPE_MP, and dCAPE_RES were calculated by

$$\text{dCAPE\_ALL} = \{\text{CAPE}[T(t + \Delta t), Q_v(t + \Delta t)] - \text{CAPE}[T(t), Q_v(t)]\}/\Delta t,$$

$$\text{dCAPE\_ADV} = \{\text{CAPE}[T(t) + \text{adv}(T)\Delta t, Q_v(t) + \text{adv}(Q_v)\Delta t] - \text{CAPE}[T(t), Q_v(t)]\}/\Delta t,$$

$$\text{dCAPE\_MP} = \{\text{CAPE}[T(t) + \text{MP}(T)\Delta t, Q_v(t) + \text{MP}(Q_v)\Delta t] - \text{CAPE}[T(t), Q_v(t)]\}/\Delta t,$$

$$\text{dCAPE\_RES} = \text{dCAPE\_ALL} - \text{dCAPE\_ADV} - \text{dCAPE\_MP},$$

where T and Q_v are air temperature and water vapor mixing ratio, $\text{adv}(T)\Delta t$ and $\text{adv}(Q_v)\Delta t$ are the air temperature and water vapor increments due to advection over a time interval Δt, and $\text{MP}(T)\Delta t$ and $\text{MP}(Q_v)\Delta t$ are the air temperature and water vapor increments due to microphysical processes over a time interval Δt. Based on the distribution of CAPE, the strong CAPE region in front of the cold-pool boundary marked with white rectangles shown in Figure 14 was selected to calculate CAPE generation rates. Figure 15 displays time series of area-averaged dCAPE_ALL, dCAPE_ADV, dCAPE_MP, and dCAPE_RES of air parcels at different originating levels in d03 of CTRL. Before 2100 UTC 06 (0500 LST 07) May 2017, the air parcels originated below 0.6 km had a larger CAPE generation rate (Figure 15a), which was mainly attributable to the large-scale advection (Figure 15b). After 2100 UTC 06 (0500 LST 07) May 2017 when the cold-pool boundary moved to the region marked with white rectangles shown in Figure 14, updrafts and convection were triggered (Figure 14) and CAPE was released (Figure 15a). The CAPE release was mainly attributable to the microphysical processes (Figure 15c), and meanwhile, CAPE was supplemented by large-scale advective forcing (Figure 15b). Besides, the air parcels originating near the surface had positive dCAPE_RES due to the heat flux from warm urban surfaces (Figure 15d). These results confirm again that the large-scale advection processes that maintained the sustaining moist southerly flow in the lower troposphere were crucial for the development of the severe rainfall. We found that the dynamic pressure perturbation gradient force also played an important role in these precipitation processes, which will be addressed in a separated article.
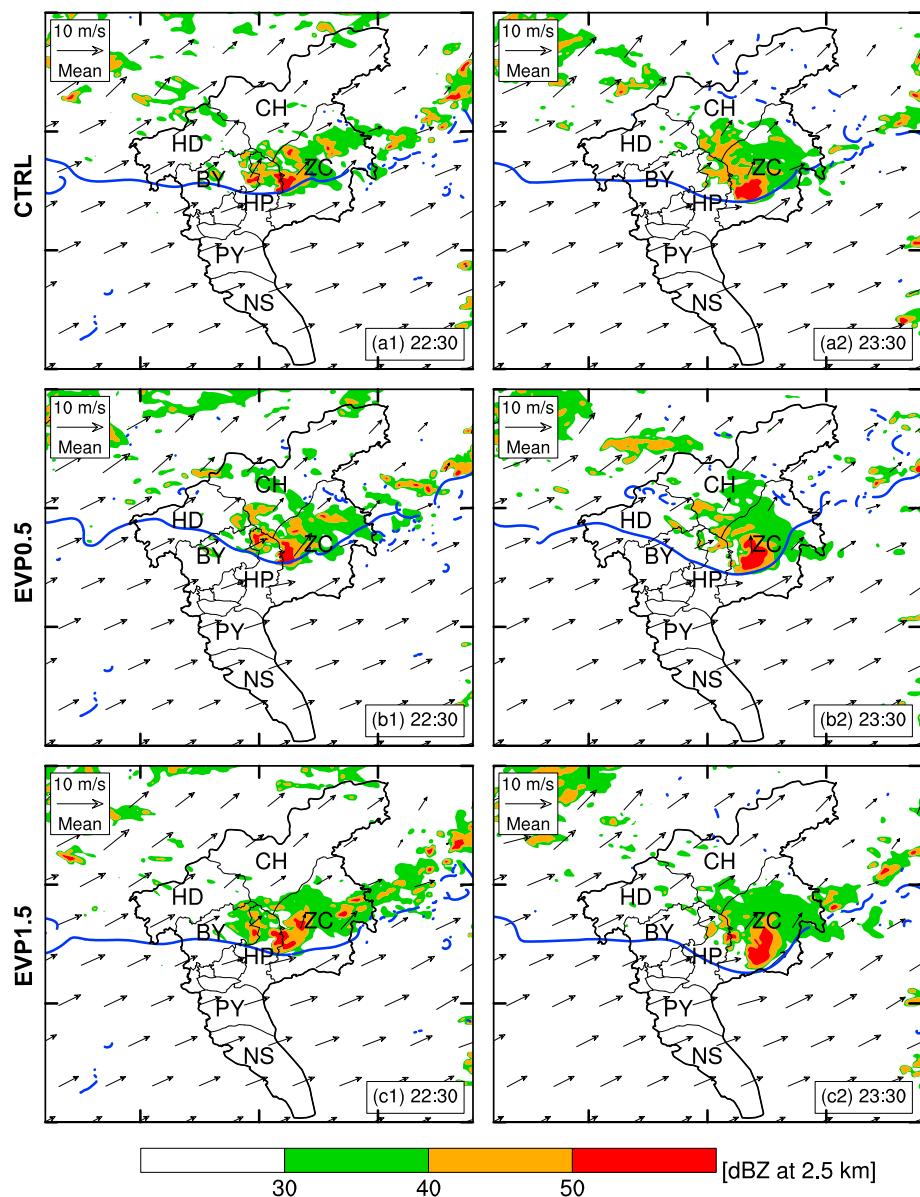
Heavy rainfall results from sustained high precipitation rates that accompany the rapid ascent of air containing substantial moisture (Doswell et al., 1996). Chappell (1986) noted that most flash floods are produced by quasi-stationary precipitation systems, wherein many convective cells reach maturity and produce their heaviest rainfall over the same area. Newton and Katz (1958) and Chappell (1986) showed that a convective

Figure 15. Time series of area-averaged CAPE generation rate (shaded in J·kg^{-1}·s^{-1}) of parcels at different originating levels from (a) all forcing (dCAPE_ALL), (b) advective forcing (dCAPE_ADV), (c) microphysical forcing (dCAPE_MP), and (d) residual forcing (dCAPE_RES) in the regions (white boxes) marked in Figure 14 from 2000 UTC 06 (0400 LST 07) May to 2300 UTC 06 (0700 LST 07) May 2017 in domain 3 of CTRL, respectively.
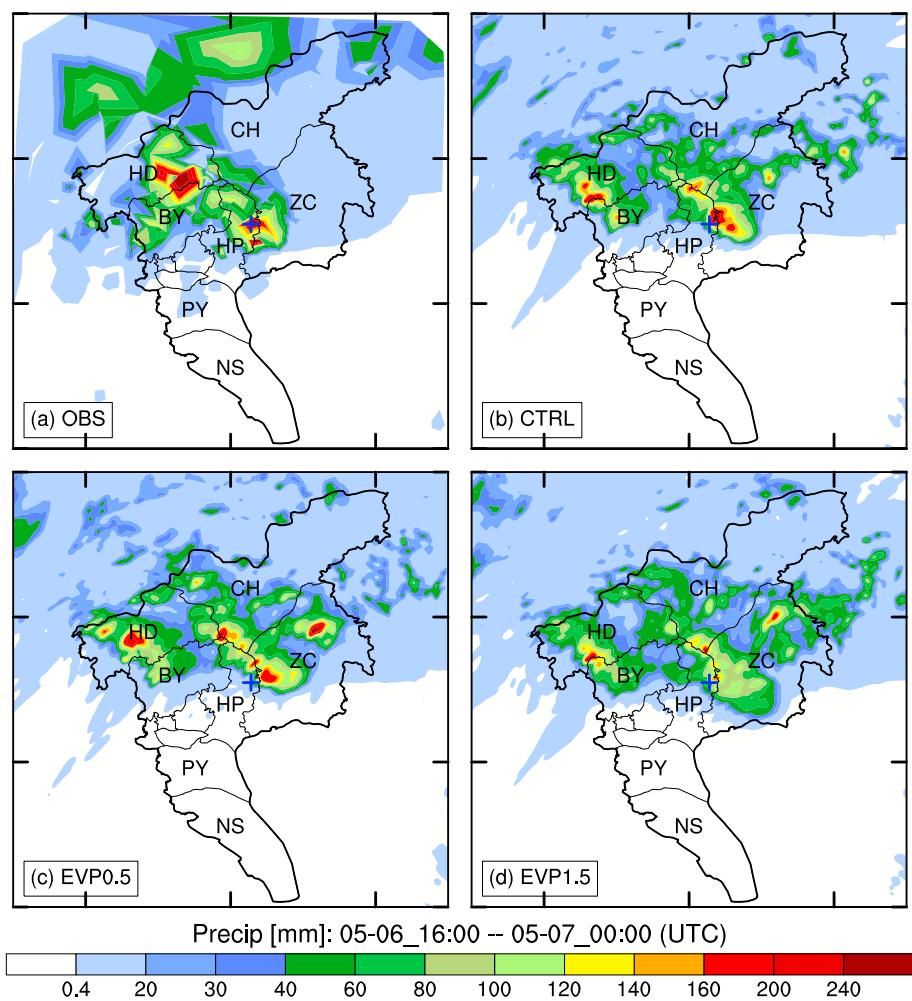
system's motion can be identified as being the vector sum of an advective component approximated by the mean cloud-layer wind (direction and magnitude) and a propagation component governed by the rate and location of new cell formation relative to existing convection. Based on this idea, a vector-based forecast technique was developed for predicting the motion of upwind- and downwind-propagating mesoscale convective systems (MCSs; Corfidi, 2003; Corfidi et al., 1996). Schumacher and Johnson (2005) examined the organization and environmental properties of extreme-rain-producing MCSs in the United States over a 3-year period and showed that extreme local rainfall is often associated with back-building/quasi-stationary MCSs, which occur when new convective cells repeatedly form upstream of their predecessors and pass over a particular area. The continuous development of upstream convection requires triggering factors, for example, frontal lifting (Schumacher et al., 2011), outflow boundaries (Houston & Wilhelmson, 2011; Houze, 2004; Jeong et al., 2016; Schumacher, 2015; Schumacher & Peters, 2017; Wang et al., 2014), interaction between the low-level jet and the midlevel circulation (mesoscale convective vortices; Schumacher, 2009; Schumacher & Johnson, 2008, 2009), orographic lifting (Duffourg et al., 2018; Soderholm et al., 2014), and thermodynamic effects associated with latent heating/cooling (Wang et al., 2016). Schumacher and Johnson (2005) also indicated that back-building/quasi-stationary MCSs are more dependent on mesoscale and storm-scale processes, particularly lifting provided by cold outflows from previous convection, than on preexisting synoptic boundaries.

To investigate the role of precipitation-generated cold outflows, two other sensitivity experiments were conducted. They are EVP0.5 and EVP1.5, in which rain water evaporation rate below 1 km above mean sea level is reduced and increased by 0.5 compared to that in CTRL, respectively. Figure 16 shows mean cloud-layer wind vectors (average of 850-, 700-, and 500-hPa wind vectors), density potential temperature θ_ρ, and radar reflectivity in d03 of CTRL, EVP0.5, and EVP1.5. The $\theta_\rho = 300$ K contours indicate the cold-pool boundaries (blue contours in Figure 16). The mean cloud-layer wind vectors show that steering flow for the convection was northeastward (Figure 16), which was the convective cells' main advection direction. Mature and decaying cells moved slowly downstream, and the cold pool also elongated in the direction of the mean wind (Figures 13 and 16). However, the cold pool's elongation was narrower in the mean wind direction in

Figure 16. Simulated mean cloud-layer wind vectors (average of 850-, 700- and 500-hPa wind vectors in m/s), density potential temperature θ_ρ (blue contour, =300 K) at 300 m above mean sea level, and radar reflectivity (shaded in dBZ) at 2.5 km above mean sea level at 2230 UTC 06 (0630 LST 07) and 2330 UTC 06 (0730 LST 07) May 2017 in domain 3 of (a1, a2) CTRL, (b1, b2) EVP0.5, and (c1, c2) EVP1.5 experiments, respectively. The thick and thin solid black lines represent Guangzhou City and its district borders, respectively. The initials in the figure are the same as those in Figure 1. Tick marks are included every 50 km.

EVP0.5 due to the weaker evaporation rate and weaker cold pool (Figures 16b1 and 16b2). In Figure 16, the southern peripheries of cold pools in ZC in CTRL and EVP0.5 were stationary and basically stayed in the center of ZC (Figures 16a1–16b2), while the southern peripheries of cold pools in ZC in EVP1.5 moved southward gradually and took 1 hr to move from the center to the southern border of ZC (Figures 16c1 and 16c2). There was a continuous supply of instability and moisture from the South China Sea (Figures 12 and 14). In CTRL, new convective cells were repeatedly triggered upstream of their predecessors (back-building process) along the quasi-stationary part of cold-pool periphery and then moved northeastward (Figures 14, 16a1, and 16a2), presenting a typical back-building convective storm structure. The stationary properties of the convection system lasted for more than 5 hr, leading to extremely heavy rainfall accumulation (Figure 17b). In EVP0.5, there was strong precipitation (Figure 17c) that was spatially
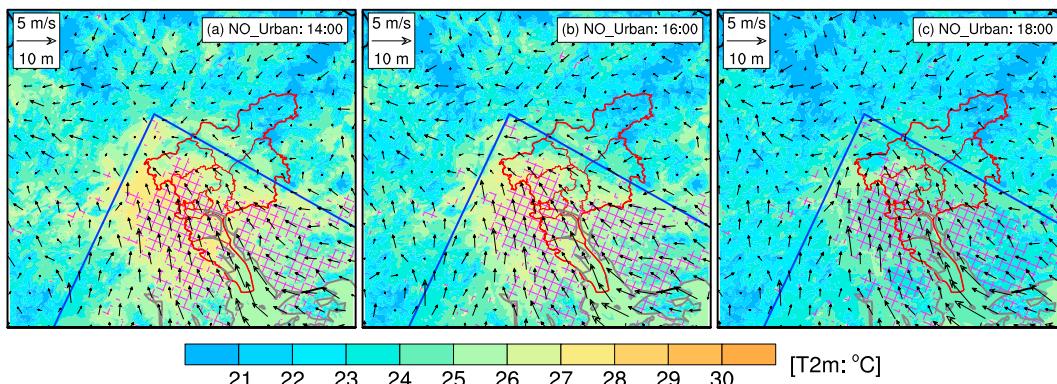
Figure 17. Accumulated precipitation (mm) in the (a) observation, (b) domain 3 of CTRL, (c) EVP0.5, and (d) EVP1.5 in the Guangzhou region from 1600 UTC 06 (0000 LST 07) May to 0000 UTC (0800 LST) 07 May 2017. The blue crosses indicate the center of maximum accumulated precipitation in the observations. The thick and thin solid black lines represent Guangzhou City and its district borders, respectively. The initials are the same as those in Figure 1. Tick marks are included every 50 km.

concentrated due to the weaker cold pool (Figures 16b1 and 16b2), while there was less accumulated precipitation in EVP1.5 (Figure 17d) resulting from the stronger cold pool. The domain-averaged accumulated precipitation in CTRL, EVP0.5, and EVP1.5 were 7.749, 7.842, and 7.744 mm, respectively, indicating the cold pool mainly influenced the distribution of precipitation. Therefore, it can be seen that the approximately balanced interaction between the precipitation-generated cold pool and the strong low-level warm, moist southerly flow played an important role in generating the observed long-lived back-building MCS and thus the extreme rainfall.
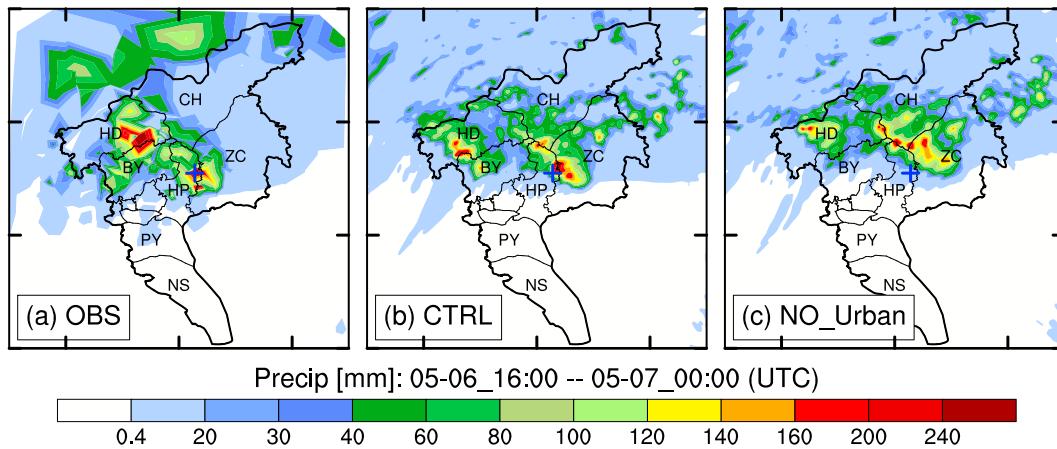
5.3. Urban Effect

To study the possible effect of the UHI of Guangzhou City on this heavy rainfall event, we conducted a sensitivity experiment, NO_Urban, in which all grid points with urban land use in the Pearl River Delta in the 0.5-km domain were replaced with cropland (which is the land use type in rural areas surrounding Guangzhou City; Figure 5d). Soil moisture and temperature were adjusted accordingly for consistency. The ICs/BCs, physical schemes, and other model settings in the NO_Urban run are identical to those of CTRL.
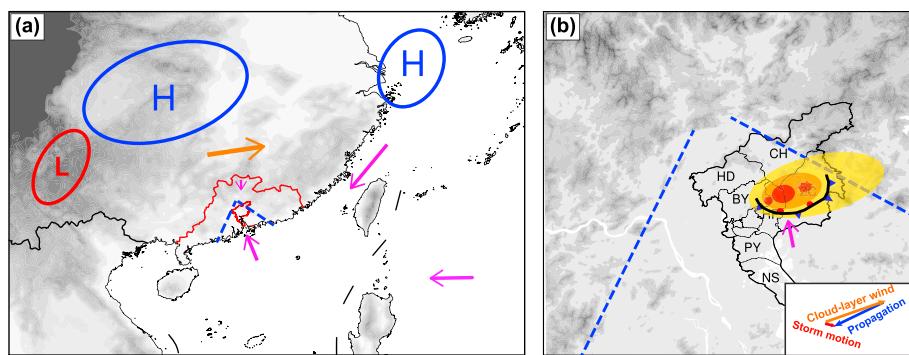
Figure 18. As in Figure 8, but for NO_Urban.

Figure 18 shows simulated wind fields at 10 m AGL and air temperature at 2 m AGL from 1400 UTC (2200 LST) 06 to 1800 UTC 06 (0200 LST 07) May 2017 in d03 of NO_Urban. Compared to that in CTRL (Figure 8), air temperature in the original urban area in NO_Urban decreased faster at night (Figure 18). However, the 10-m winds changed little. We infer this is because wind flows in this case are mainly controlled by large-scale dynamics, and the southerly wind over the Pearl River Delta does not change much just due to the decrease of air temperature near the surface layer in a short forcing period starting from 1200 UTC (2000 LST) 06 May 2017.

The simulated composite reflectivity in HD in NO_Urban reached 35 dBZ at 1630 UTC 06 (0030 LST 07) May 2017, which appeared a little (~30 min) later than that of CTRL. The location of the convection also shifted. The differences in the simulated reflectivity between CTRL and NO_Urban were mostly before 1900 UTC 06 (0300 LST 07) May. After that, the simulations resembled each other. The hourly accumulated precipitation in the two simulations were slightly offset, but the precipitation intensity and temporal evolution were very similar. From the accumulated precipitation shown in Figure 19, the accumulated precipitation of CTRL is more concentrated, and the maximum accumulated precipitation center is more consistent with observation than that of NO_Urban. Though NO_Urban simulated faster decrease of the air temperature at 2 m AGL at night (Figure 18), the southerly flow in the lower troposphere, which was mainly controlled by synoptic forcing discussed in section 4.1, was only marginally affected. The severe convective storms were still produced in No_Urban (Figure 19c) with similar rainfall as in CTRL (Figure 19b). Therefore, for this case, evidence suggests that urban forcing was not a necessary factor for the initiation and development of severe

Figure 19. Accumulated precipitation (mm) in the (a) observations, (b) domain 3 of CTRL, and (c) NO_Urban in the Guangzhou region from 1600 UTC 06 (0000 LST 07) May to 0000 UTC (0800 LST) 07 May 2017. The blue crosses indicate the center of maximum accumulated precipitation in the observations. The thick and thin solid black lines represent Guangzhou City and its district borders, respectively. The initials are the same as those in Figure 1. Tick marks are included every 50 km.

Figure 20. Schematic diagram of the main characteristics of the severe rainfall event, 6−7 May 2017 in Guangzhou: (a) favorable synoptic and mesoscale patterns and topographic features and (b) long-lasting quasi-stationary convective system. Shown in (a) are terrain elevation (shaded; the deeper gray, the higher the elevation), cold highs (blue ellipses) and warm low (red ellipse) in the lower troposphere, and wind vectors in the lower (magenta vectors) and upper (orange vector) troposphere. Shown in (b) are terrain elevation (shaded, same as in (a)), wind vector in the lower troposphere (magenta vector), radar reflectivity (shaded ellipses), and motion of the cold-pool boundary depicted by conventional frontal symbols. The diagram in the bottom right of (b) shows the mechanism for back-building mesoscale convective systems (vector synthesis of orange, blue, and red vectors). The blue dashed lines in (a) and (b) mark the trumpet-shaped topography.

convection, but urban forcing did slightly influence the timing and location of convection and helped to concentrate the maximum rain in a manner more consistent with observations.

5.4. Conceptual Model of the Heavy Precipitation

According to the above analysis of the heavy rainfall mechanisms, Figure 20 sketches a conceptual model. Three important factors affected the development of torrential rainfall. They are favorable synoptic and mesoscale patterns, topographic effects, and cold pools. The favorable synoptic and mesoscale patterns and the trumpet-shaped topographic features of the Pearl River Delta resulted in important sustained warm moist southerly flows in the lower troposphere that supplied fuel for the convective storms over Guangzhou (Figure 20a). The circulation pattern provided very favorable conditions for the accumulation of CAPE and triggering initial convection. The development of the initial convection strengthened the convergence in the lower levels, and the southerly flow further strengthened, which continuously brought plentiful water vapor to support the continuing development of the heavy rainfall in the region. The cold-pool outflow boundaries of the convection storms helped trigger new convection at the quasi-stationary part of the cold-pool boundaries when they met the warm moist southerly flow, maintaining a back-building quasi-stationary rainfall system, and thus led to extreme rainfall in ZC (Figure 20b). Although the urban forcing was only a secondary driving factor for the overall system development, it affected the timing of convective initiation and the location and the rainfall intensity.

6. Summary and Conclusions

In this study, the mechanisms for a record-breaking rainfall in the coastal metropolitan city of Guangzhou, China, during 6–7 May 2017 were studied with observational analysis and nested VLESs with the WRF model. We found that the key factors affecting the development of torrential rainfall included favorable environmental conditions (synoptic and mesoscale patterns and topographic effects), cold pools, and, to a lesser extent, urban effects. The major findings are summarized as follows.

1. The combination of the relatively slowly evolving synoptic and mesoscale patterns and the unique topographic features of the Pearl River Delta generated and maintained the warm moist southerly flow in the lower troposphere and supplied fuel for the convective storms over Guangzhou. With the initial convective development, the southerly flow strengthened and continuously brought abundant water vapor to support the heavy rainfall in the region.
2. The CAPE development in the extreme rainfall region between HP and ZC Districts was maintained by the sustaining moist southerly flow in the lower troposphere and large-scale advection in the middle and upper layers, coincident with release of latent heat in these layers.

3. The matching interaction between the precipitation-produced cold-pool outflows and warm moist southerly flow repeatedly triggered new convection upstream at the quasi-stationary part of the cold-pool boundaries, resulting in a back-building quasi-stationary MCS, causing extreme local rainfall in ZC.

4. The influence of urban forcing on this heavy rain event is secondary. However, urban forcing did help earlier initiation of the convection and concentrated it to produce a higher rainfall maximum.

These results indicate the importance of understanding synoptic and mesoscale dynamics and the influence of topography in forecasting rare but extreme heavy rainfall. In such cases, forecasters ought to assess the southerly lower tropospheric flow and the magnitude of water vapor and thermal fluxes and their duration, midlayer wind profiles, and potential convection cold-pool intensity in order to predict such heavy rain events. The successful simulation of this case using nested VLESs with the WRF model indicates that sub-kilometer-scale numerical weather prediction without boundary-layer parameterizations is promising in certain situations for providing valuable guidance for heavy rainfall forecasts in urban areas.

Further work on quantitative analysis of this case's dynamical processes and a budget computation to investigate the thermodynamic forcing and moisture processes is ongoing. We found that an important role might have been played by dynamical pressure forces that supported the development of significant updrafts and the heavy rainfall. In addition, urban areas can produce a large amount of pollution, which can influence cloud microphysical processes, radiative processes, and surface precipitation (Rosenfeld et al., 2008; Van Den Heever & Cotton, 2007). On the other hand, the southern side of Guangzhou City is opened to the South China Sea where the sea salt aerosols can be brought into Guangzhou City by the southerly wind. Work has been undertaken to explore how these aerosols might have affected the precipitation development in this event. The results of these studies will be reported in two separated papers.

References

Balk, D., McGranahan, G., & Anderson, B. (2008). Urbanization and ecosystems: Current patterns and future implications. In G. Martine, et al. (Eds.), *The new global frontier: Urbanization, poverty and environment in the 21st century* (pp. 183–201). London, UK: Earthscan.

Beaudoing, H., & Rodell, M. (2016). GLDAS Noah land surface model L4 3 hourly 0.25 × 0.25 degree V2.1, Greenbelt, Maryland, USA, Goddard Earth Sciences Data and Information Services Center (GES DISC), Accessed 01 Jan 2018. https://doi.org/10.5067/ E7TYRXPJKWOQ

Bornstein, R., & Lin, Q. (2000). Urban heat islands and summertime convective thunderstorms in Atlanta: Three case studies. *Atmospheric Environment*, *34*(3), 507–516. https://doi.org/10.1016/S1352-2310(99)00374-X

Bryan, G. H., Wyngaard, J. C., & Fritsch, J. M. (2003). Resolution requirements for the simulation of deep moist convection. *Monthly Weather Review*, *131*(10), 2394–2416. https://doi.org/10.1175/1520-0493(2003)131<2394:RRFTSO>2.0.CO;2

Chappell, C. F. (1986). Quasi-stationary convective events. In P. S. Ray (Ed.), *Mesoscale meteorology and forecasting* (pp. 289–310). Boston, MA: American Meteorological Society. https://doi.org/10.1007/978-1-935704-20-1_13

Chen, G., Yoshida, R., Sha, W., Iwasaki, T., & Qin, H. (2014). Convective instability associated with the eastward-propagating rainfall episodes over eastern China during the warm season. *Journal of Climate*, *27*(6), 2331–2339. https://doi.org/10.1175/JCLI-D-13-00443.1

Chu, X., Geerts, B., Xue, L., & Pokharel, B. (2017). A case study of cloud radar observations and large-eddy simulations of a shallow Stratiform orographic cloud, and the impact of glaciogenic seeding. *Journal of Applied Meteorology and Climatology*, *56*(5), 1285–1304. https://doi.org/10.1175/JAMC-D-16-0364.1

Chu, X., Xue, L., Geerts, B., Rasmussen, R., & Breed, D. (2014). A case study of radar observations and WRF LES simulations of the impact of ground-based glaciogenic seeding on orographic clouds and precipitation. Part I: Observations and model validations. *Journal of Applied Meteorology and Climatology*, *53*(10), 2264–2286. https://doi.org/10.1175/JAMC-D-14-0017.1

Corfidi, S. F. (2003). Cold pools and MCS propagation: Forecasting the motion of downwind-developing MCSs. *Weather and Forecasting*, *18*(6), 997–1017. https://doi.org/10.1175/1520-0434(2003)018<0997:CPAMPF>2.0.CO;2

Corfidi, S. F., Meritt, J. H., & Fritsch, J. M. (1996). Predicting the movement of mesoscale convective complexes. *Weather and Forecasting*, *11*(1), 41–46. https://doi.org/10.1175/1520-0434(1996)011<0041:PTMOMC>2.0.CO;2

Doswell, C. A. III, Brooks, H. E., & Maddox, R. A. (1996). Flash flood forecasting: An ingredients-based methodology. *Weather and Forecasting*, *11*(4), 560–581. https://doi.org/10.1175/1520-0434(1996)011<0560:FFFAIB>2.0.CO;2

Dou, J., Wang, Y., Bornstein, R., & Miao, S. (2015). Observed spatial characteristics of Beijing urban climate impacts on summer thunderstorms. *Journal of Applied Meteorology and Climatology*, *54*(1), 94–105. https://doi.org/10.1175/JAMC-D-13-0355.1

Duffourg, F., Lee, K. O., Ducrocq, V., Flamant, C., Chazette, P., & Di Girolamo, P. (2018). Role of moisture patterns in the backbuilding formation of HyMeX IOP13 heavy precipitation systems. *Quarterly Journal of the Royal Meteorological Society*, *144*(710), 291–303. https://doi.org/10.1002/qj.3201

Emanuel, K. A. (1994). *Atmospheric Convection*. New York: Oxford University Press.

Grimm, N. B., Faeth, S. H., Golubiewski, N. E., Redman, C. L., Wu, J., Bai, X., & Briggs, J. M. (2008). Global change and the ecology of cities. *Science*, *319*(5864), 756–760. https://doi.org/10.1126/science.1150195

Han, J. Y., & Baik, J. J. (2008). A theoretical and numerical study of urban heat island-induced circulation and convection. *Journal of the Atmospheric Sciences*, *65*(6), 1859–1877. https://doi.org/10.1175/2007JAS2326.1

Heath, N. K., Fuelberg, H. E., Tanelli, S., Turk, F. J., Lawson, R. P., Woods, S., & Freeman, S. (2017). WRF nested large-eddy simulations of deep convection during SEAC4RS. *Journal of Geophysical Research: Atmospheres*, *122*, 3953–3974. https://doi.org/10.1002/2016JD025465

Hong, S. Y., & Lim, J. J. (2006). The WRF single-moment 6-class microphysics scheme (WSM6). *Journal of the Korean Meteorological Society*, *42*(2), 129–151.

Houston, A. L., & Wilhelmson, R. B. (2011). The dependence of storm longevity on the pattern of deep convection initiation in a low-shear environment. *Monthly Weather Review*, *139*(10), 3125–3138. https://doi.org/10.1175/MWR-D-10-05036.1

Houze, R. A. Jr. (2004). Mesoscale convective systems. *Reviews of Geophysics*, *42*, RG4003. https://doi.org/10.1029/2004RG000150

Huang, Y., Liu, Y., Xu, M., Liu, Y., Pan, L., Wang, H., Cheng, W. Y. Y., et al. (2018). Forecasting severe convective storms with WRF-based RTFDDA radar data assimilation in Guangdong, China. *Atmospheric Research*, *209*, 131–143. https://doi.org/10.1016/j.atmosres.2018.03.010

Iacono, M. J., Delamere, J. S., Mlawer, E. J., Shephard, M. W., Clough, S. A., & Collins, W. D. (2008). Radiative forcing by long-lived greenhouse gases: Calculations with the AER radiative transfer models. *Journal of Geophysical Research*, *113*, D13103. https://doi.org/10.1029/2008JD009944

Jeong, J. H., Lee, D. I., & Wang, C. C. (2016). Impact of the cold pool on mesoscale convective system-produced extreme rainfall over southeastern South Korea: 7 July 2009. *Monthly Weather Review*, *144*(10), 3985–4006. https://doi.org/10.1175/MWR-D-16-0131.1

Kang, S. L., & Bryan, G. H. (2011). A large-eddy simulation study of moist convection initiation over heterogeneous surface fluxes. *Monthly Weather Review*, *139*(9), 2901–2917. https://doi.org/10.1175/MWR-D-10-05037.1

Liu, Y., Warner, T., Liu, Y., Vincent, C., Wu, W., Mahoney, B., Swerdlin, S., et al. (2011). Simultaneous nested modeling from the synoptic scale to the LES scale for wind energy applications. *Journal of Wind Engineering and Industrial Aerodynamics*, *99*(4), 308–319. https://doi.org/10.1016/j.jweia.2011.01.013

Liu, Y., Warner, T. T., Astling, E. G., Bowers, J. F., Davis, C. A., Halvorson, S. F., et al. (2008). The operational mesogamma-scale analysis and forecast system of the US Army test and evaluation command. Part II: Interrange comparison of the accuracy of model analyses and forecasts. *Journal of Applied Meteorology and Climatology*, *47*(4), 1093–1104. https://doi.org/10.1175/2007JAMC1654.1

Liu, Y., Warner, T. T., Bowers, J. F., Carson, L. P., Chen, F., Clough, C. A., et al. (2008). The operational mesogamma-scale analysis and forecast system of the US Army Test and Evaluation Command. Part I: Overview of the modeling system, the forecast products, and how the products are used. *Journal of Applied Meteorology and Climatology*, *47*(4), 1077–1092. https://doi.org/10.1175/2007JAMC1653.1

Miao, S., Chen, F., Li, Q., & Fan, S. (2011). Impacts of urban processes and urbanization on summer precipitation: A case study of heavy rainfall in Beijing on 1 August 2006. *Journal of Applied Meteorology and Climatology*, *50*(4), 806–825. https://doi.org/10.1175/2010JAMC2513.1

Morrison, H., Thompson, G., & Tatarskii, V. (2009). Impact of cloud microphysics on the development of trailing stratiform precipitation in a simulated squall line: Comparison of one- and two-moment schemes. *Monthly Weather Review*, *137*(3), 991–1007. https://doi.org/10.1175/2008MWR2556.1

Newton, C. W., & Katz, S. (1958). Movement of large convective rainstorms in relation to winds aloft. *Bulletin of the American Meteorological Society*, *39*(3), 129–136. https://doi.org/10.1175/1520-0477-39.3.129

Niyogi, D., Pyle, P., Lei, M., Arya, S. P., Kishtawal, C. M., Shepherd, M., et al. (2011). Urban modification of thunderstorms: An observational storm climatology and model case study for the Indianapolis urban region. *Journal of Applied Meteorology and Climatology*, *50*(5), 1129–1144. https://doi.org/10.1175/2010JAMC1836.1

Panosetti, D., Böing, S., Schlemmer, L., & Schmidli, J. (2016). Idealized large-eddy and convection-resolving simulations of moist convection over mountainous terrain. *Journal of the Atmospheric Sciences*, *73*(10), 4021–4041. https://doi.org/10.1175/JAS-D-15-0341.1

Parodi, A., & Tanelli, S. (2010). Influence of turbulence parameterizations on high-resolution numerical modeling of tropical convection observed during the TC4 field campaign. *Journal of Geophysical Research*, *115*, D00J14. https://doi.org/10.1029/2009JD013302

Roberts, N. M., & Lean, H. W. (2008). Scale-selective verification of rainfall accumulations from high-resolution forecasts of convective events. *Monthly Weather Review*, *136*(1), 78–97. https://doi.org/10.1175/2007MWR2123.1

Rosenfeld, D., Lohmann, U., Raga, G. B., O'dowd, C. D., Kulmala, M., Fuzzi, S., et al. (2008). Flood or drought: How do aerosols affect precipitation? *Science*, *321*(5894), 1309–1313. https://doi.org/10.1126/science.1160606

Schumacher, R. S. (2009). Mechanisms for quasi-stationary behavior in simulated heavy-rain-producing convective systems. *Journal of the Atmospheric Sciences*, *66*(6), 1543–1568. https://doi.org/10.1175/2008JAS2856.1

Schumacher, R. S. (2015). Sensitivity of precipitation accumulation in elevated convective systems to small changes in low-level moisture. *Journal of the Atmospheric Sciences*, *72*(6), 2507–2524. https://doi.org/10.1175/JAS-D-14-0389.1

Schumacher, R. S., Galarneau, T. J. Jr., & Bosart, L. F. (2011). Distant effects of a recurving tropical cyclone on rainfall in a midlatitude convective system: A high-impact predecessor rain event. *Monthly Weather Review*, *139*(2), 650–667. https://doi.org/10.1175/2010MWR3453.1

Schumacher, R. S., & Johnson, R. H. (2005). Organization and environmental properties of extreme-rain-producing mesoscale convective systems. *Monthly Weather Review*, *133*(4), 961–976. https://doi.org/10.1175/MWR2899.1

Schumacher, R. S., & Johnson, R. H. (2008). Mesoscale processes contributing to extreme rainfall in a midlatitude warm-season flash flood. *Monthly Weather Review*, *136*(10), 3964–3986. https://doi.org/10.1175/2008MWR2471.1

Schumacher, R. S., & Johnson, R. H. (2009). Quasi-stationary, extreme-rain-producing convective systems associated with midlevel cyclonic circulations. *Weather and Forecasting*, *24*(2), 555–574. https://doi.org/10.1175/2008WAF2222173.1

Schumacher, R. S., & Peters, J. M. (2017). Near-surface thermodynamic sensitivities in simulated extreme-rain-producing mesoscale convective systems. *Monthly Weather Review*, *145*(6), 2177–2200. https://doi.org/10.1175/MWR-D-16-0255.1

Seino, N., Aoyagi, T., & Tsuguti, H. (2018). Numerical simulation of urban impact on precipitation in Tokyo: How does urban temperature rise affect precipitation? *Urban Climate*, *23*, 8–35. https://doi.org/10.1016/j.uclim.2016.11.007

Shepherd, J. M. (2005). A review of current investigations of urban-induced rainfall and recommendations for the future. *Earth Interactions*, *9*(12), 1–27. https://doi.org/10.1175/EI156.1

Shin, H. H., & Hong, S. Y. (2015). Representation of the subgrid-scale turbulent transport in convective boundary layers at gray-zone resolutions. *Monthly Weather Review*, *143*(1), 250–271. https://doi.org/10.1175/MWR-D-14-00116.1

Soderholm, B., Ronalds, B., & Kirshbaum, D. J. (2014). The evolution of convective storms initiated by an isolated mountain ridge. *Monthly Weather Review*, *142*(4), 1430–1451. https://doi.org/10.1175/MWR-D-13-00280.1

Suhas, E., & Zhang, G. J. (2014). Evaluation of trigger functions for convective parameterization schemes using observations. *Journal of Climate*, *27*(20), 7647–7666. https://doi.org/10.1175/JCLI-D-13-00718.1

Tewari, M., Chen, F., Wang, W., Dudhia, J., LeMone, M. A., Mitchell, K., et al. (2004). Implementation and verification of the unified Noah land surface model in the WRF model. Paper presented at 20th Conference on Weather Analysis and Forecasting/16th Conference on

Numerical Weather Prediction, American Meteorological Society, Seattle, WA. Retrieved from https://ams.confex.com/ams/84Annual/techprogram/paper_69061.htm

Thompson, G., Field, P. R., Rasmussen, R. M., & Hall, W. D. (2008). Explicit forecasts of winter precipitation using an improved bulk microphysics scheme. Part II: Implementation of a new snow parameterization. *Monthly Weather Review*, *136*(12), 5095–5115. https://doi.org/10.1175/2008MWR2387.1

United Nations (2016). *The world's cities in 2016*. United Nations, Department of Economic and Social Affairs, Population Division, New York, NY. Retrieved from http://www.un.org/en/development/desa/population/publications/pdf/urbanization/the_worlds_cities_in_2016_data_booklet.pdf

Van Den Heever, S. C., & Cotton, W. R. (2007). Urban aerosol impacts on downwind convective storms. *Journal of Applied Meteorology and Climatology*, *46*(6), 828–850. https://doi.org/10.1175/JAM2492.1

Wang, C. C., Chiou, B. K., Chen, G. T. J., Kuo, H. C., & Liu, C. H. (2016). A numerical study of back-building process in a quasistationary rainband with extreme rainfall over northern Taiwan during 11–12 June 2012. *Atmospheric Chemistry and Physics*, *16*(18), 12,359–12,382.

Wang, H., Luo, Y., & Jou, B. J. D. (2014). Initiation, maintenance, and properties of convection in an extreme rainfall event during SCMREX: Observational analysis. *Journal of Geophysical Research: Atmospheres*, *119*, 13,206–13,232. https://doi.org/10.1002/2014JD022339

Wyngaard, J. C. (2004). Toward numerical modeling in the "terra incognita." *Journal of the Atmospheric Sciences*, *61*, 1816–1826. https://doi.org/10.1175/1520-0469(2004)061<1816:TNMITT>2.0.CO;2

Xie, S., & Zhang, M. H. (2000). Impact of the convection triggering function on single-column model simulations. *Journal of Geophysical Research*, *105*(D11), 14983–14996. https://doi.org/10.1029/2000JD900170

Xue, L., Chu, X., Rasmussen, R., Breed, D., & Geerts, B. (2016). A case study of radar observations and WRF LES simulations of the impact of ground-based glaciogenic seeding on orographic clouds and precipitation. Part II: AgI dispersion and seeding signals simulated by WRF. *Journal of Applied Meteorology and Climatology*, *55*(2), 445–464. https://doi.org/10.1175/JAMC-D-15-0115.1

Xue, L., Edwards, R., Huggins, A., Lou, X., Rasmussen, R., Tessendorf, S., et al. (2017). WRF large-eddy simulations of chemical tracer deposition and seeding effect over complex terrain from ground-and aircraft-based AgI generators. *Atmospheric Research*, *190*, 89–103. https://doi.org/10.1016/j.atmosres.2017.02.013

Zhang, D., & Anthes, R. A. (1982). A high-resolution model of the planetary boundary layer—Sensitivity tests and comparisons with SESAME-79 data. *Journal of Applied Meteorology*, *21*(11), 1594–1609. https://doi.org/10.1175/1520-0450(1982)021<1594:AHRMOT>2.0.CO;2

Zhang, G. J. (2002). Convective quasi-equilibrium in midlatitude continental environment and its effect on convective parameterization. *Journal of Geophysical Research*, *107*(D14), 4220. https://doi.org/10.1029/2001JD001005